Supplemental Information

Progress and Perspectives of Electrochemical CO_2 Reduction on Copper in Aqueous Electrolyte

Stephanie Nitopi,[a,~] Erlend Bertheussen,[b,~] Soren B. Scott,[b] Xinyan Liu,[a] Albert K. Engstfeld,[b,c] Sebastian Horch,[b] Brian Seger,[b] Ifan E.L. Stephens,[b,e] Karen Chan,[a,d] Christopher Hahn,[a,d] Jens K. Nørskov,[a,b,d,*] Thomas F. Jaramillo,[a,d,*] and Ib Chorkendorff[b,*]

[a] SUNCAT Center for Interface Science and Catalysis, Department of Chemical Engineering, Stanford University, Stanford, California 94305, United States
[b] Section for Surface Physics and Catalysis, Department of Physics, Technical University of Denmark, 2800 Kgs. Lyngby, Denmark
[c] Institute of Surface Chemistry and Catalysis, Ulm University, D-89069 Ulm, Germany
[d] SUNCAT Center for Interface Science and Catalysis, SLAC National Accelerator Laboratory, Menlo Park, California 94025, United States
[e] Department of Materials, Imperial College London, Royal School of Mines, London SW7 2AZ, U.K.

Table of Contents

1 Thermochemistry: Raw Data and Calculations

1.1 Thermochemistry Data for Carbon Products and Copper Phases

Table S1: **Thermochemistry data for carbon products and copper phases**

Name	Compound	$\Delta_f G^\circ$ / kJ mol^{-1}	$\Delta_f H^\circ$ / kJ mol^{-1}	S° / J K^{-1} mol^{-1}	K_H / bar M^{-1}
Hydrogen	H_2(g)	0	0	130.7 [a]	
Graphite	C(s)	0	0	5.6 [a]	
Oxygen	O_2(g)	0	0	205.2 [a]	
Water	H_2O(l)	-237.1 [*]	-285.8 [a]	70.0 [a]	
Carbon Dioxide	CO_2(g)	-394.4 [*]	-393.5 [a]	213.8 [a]	
Carbon Products					
Carbon Monoxide	CO(g)	-137.2 [*]	-110.5 [a]	197.7 a	
Formic Acid	HCOOH(g)	-350.9 [*]	-378.6 [a]	248.7 [a]	
	HCOOH(aq)	-372.3 [*]			1.7810-4 [a]
Methanol	CH_3OH(g)	-162.3 [b]	-201.2 [b]	126.8 [b]	
	CH_3OH(aq)	-175.7 [*]			4.5510-3 [a]
Methane	CH_4(g)	-50.9 [*]	-74.9 [a]	186.7 [a]	
Oxalic Acid	$(COOH)_2$(s)	-698.9 [*]	-829 [a]	116 [a]	
Acetic Acid	CH_3COOH(g)	-374.9 [*]	-433 [a]	282.8 [a]	
	CH_3COOH(aq)	-396.3 [*]			1.8210-4 [a]
Acetaldehyde	CH_3CHO(g)	-133.0 [b]	-166.1 [b]	263.8 [b]	
	CH_3CHO(aq)	-139.7 [*]			6.6710-2 [a]
Ethanol	CH_3CH_2OH(g)	-167.9 [b]	-234.8 [b]	281.6 [b]	
	CH_3CH_2OH(aq)	-181.3 [*]			4.5510-3 [a]
Ethylene	C_2H_4(g)	68.3 [*]	52.4 [a]	219.3 [a]	
Propionaldehyde	CH_3CH_2CHO(g)	-127.0 [*]	-188.7 [a]	304.4 [a]	
	CH_3CH_2CHO(aq)	-133.3 [*]			7.6910-2 [a]
1-Propanol	$CH_3CH_2CH_2OH$(g)	-160.7 [*]	-256 [a]	322.5 [a]	
	$CH_3CH_2CH_2OH$(aq)	-173.0 [*]			7.1410-3 [a]
Copper Phases					
Copper	Cu(s)	0	0	33.2 [a]	
Cuprous Oxide	Cu_2O(s)	-147.9 [*]	-170.7 [a]	92.4 [a]	
Cupric Oxide	CuO(s)	-128.3 [*]	-156.1 [a]	42.6 [a]	
Copper Hydroxide	$Cu(OH)_2$(s)	-372.6 [*]	-450 [a]	108.4 [a]	
Malachite	$Cu_2(CO_3)(OH)_2$(s)	-894.00 [c]			

Sources:
[a], NIST Chemistry Webbook, `https://webbook.nist.gov/chemistry/`. For Henrys-Law data, the units were converted from mol/(kg·bar) to bar·l/mol = bar/M by taking the reciprocal of the median reliable reported value.
[b], John A. Dean, Langes Handbook of Chemistry Fifteenth Edition, McGraw-Hill Inc, 1999.
[c], Kiseleva et al, Thermodynamic Properties of Copper Carbonates - Malachite $Cu_2(OH)_2CO_3$ and Azurite $Cu_3(OH)_2(CO_3)_2$. *Physics and Chemistry of Materials*, 1992.
[*], Calculated from the other data in the table.

Table S1 shows the raw and derived thermochemical data used to calculate the equilibrium potentials included in Tables 2 and 5 of this work. The superscript indicates the source, whereas an asterisk indicates a value we calculated from the raw data reported in the table as described below. Whenever possible, we used the standard enthalpy of formation ($\Delta_f H^\circ$) and standard entropy (S°) from NIST Chemistry Webbook. For methanol, acetaldehyde, and ethanol, the standard entropy is missing from the gas-phase thermochemistry data from NIST, and so we used the Langes Handbook of Chemistry for both $\Delta_f H^\circ$ and S°. Only one compound of interest, malachite (copper carbonate dihydroxide, $Cu_2CO_3(OH)_2(s)$), was not in either of these compilations, and its free energy of formation was therefore taken from an original work (Kiseleva, 1992). For aqueous products, we also looked up the Henrys law constant from NIST. NIST uses the compilation by Sanders (Sanders, 1999), which lists several primary sources for each compound with an indication of how reliable each one is. We used the median reliable value (indication 'M' or 'L'), and take the reciprocal to get the units the table.

The quantities of interest for calculating chemical equilibria, including standard electrochemical reduction potentials, are the free energy of formation of the reactants and products ($\Delta_f G^\circ$). The free energy of formation is related to the standard enthalpy of formation ($\Delta_f H^\circ$) and standard entropy of formation ($\Delta_f S^\circ$) according to

$$\Delta_f G^\circ = \Delta_f H^\circ - T^\circ \Delta_f S^\circ \,, \tag{1}$$

where T = 298.15 K is the standard thermodynamic temperature, 25C. The standard entropy of formation is not tabulated, but can be calculated by the tabulated absolute standard entropies (S°) by

$$\Delta_f S^\circ = \Sigma \nu_i S_i^\circ \,, \tag{2}$$

where i is the stoichiometric coefficient for species i in the formation reaction, which is the theoretical reaction forming the compound from its constituent elements in their standard states. As an example, we consider propionaldehyde. The formation reaction for gaseous propionaldehyde ($\mathrm{CH_3CH_2CHO\,(g)}$) is

$$3\,\mathrm{C_{(s)}} + 3\,\mathrm{H_{2\,(g)}} + \frac{1}{2}\,\mathrm{O_{2\,(g)}} \longrightarrow \mathrm{CH_3CH_2CHO_{(g)}} \,, \tag{3}$$

and the standard entropy of formation is

$$\begin{aligned} \Delta_f S^\circ_{\mathrm{CH_3CH_2CHO\,(g)}} &= S^\circ_{\mathrm{CH_3CH_2CHO\,(g)}} - 3S^\circ_{\mathrm{C\,(s)}} - 3S^\circ_{\mathrm{H_2\,(g)}} - \frac{1}{2}S^\circ_{\mathrm{O_2\,(g)}} && (4) \\ &= \left(304.4 - 3\cdot 5.6 - 3\cdot 130.7 - \frac{1}{2}\cdot 205.2\right)\frac{\mathrm{J}}{\mathrm{mol\cdot K}} && (5) \\ &= -207.0\frac{\mathrm{J}}{\mathrm{mol\cdot K}} \,. && (6) \end{aligned}$$

The free energy of formation for gaseous propionaldehyde is then

$$\Delta_f G^\circ_{\mathrm{CH_3CH_2CHO\,(g)}} = -188.7\frac{\mathrm{kJ}}{\mathrm{mol}} - 298.15\mathrm{K}\cdot\left(-207.0\frac{\mathrm{J}}{\mathrm{mol\cdot K}}\right) = -127.0\frac{\mathrm{kJ}}{\mathrm{mol}} \,. \tag{7}$$

This report considers reduction of CO_2 in aqueous electrolyte. We therefore consider liquid CO_2 reduction products in their solvated state (the standard state being the extrapolation from infinitely dilute solutions up to 1 mol/l = 1 M). Given the available data, the most convenient and reliable way to obtain free energies of formation for aqueous products is to adjust for the free energy of solvation of the gas-phase product ($\Delta_{g\to aq} G^\circ$). This is related to the Henrys-law constant (K_H) by

$$\Delta_{\mathrm{g\to aq}} G^\circ = RT^\circ \ln(K_H) \,, \tag{8}$$

since the Henrys-law constant is the equilibrium constant for the reverse reaction (thus the lack of a minus sign). Note that the Henrys-law constant in this equation must be dimensionless, i.e. activity-based, but that it is numerically equivalent to that in Table S1 because 1 bar (idealized) is the standard state of a gas and 1 M (idealized) is the standard state of a solvated compound. The free energy of formation of aqueous propionaldehyde is then

$$\begin{aligned} \Delta_f G^\circ_{\mathrm{CH_3CH_2CHO\,(aq)}} &= \Delta_f G^\circ_{\mathrm{CH_3CH_2CHO\,(g)}} + \Delta_{\mathrm{g\to aq}} G^\circ_{\mathrm{CH_3CH_2CHO}} && (9) \\ &= -127.0\frac{\mathrm{kJ}}{\mathrm{mol}} + RT^\circ \ln\left(7.69\cdot 10^{-2}\right) && (10) \\ &= -133.3\frac{\mathrm{kJ}}{\mathrm{mol}} \,. && (11) \end{aligned}$$

The free energies of formation for all the other compounds were derived using the same procedure.

1.2 Calculation of Equilibrium Potentials

$\mathbf{CO_2}$ Reduction

In general, the electrochemical reduction of CO_2 is described by the equation

$$x\,CO_2 + n\,(H^+ + e^-) \longrightarrow \text{Product} + y\,H_2O\,. \tag{12}$$

The free energy change of this reaction with H_2O, CO_2, and Product in their standard states is

$$\Delta_{CO_2R}G^\circ = \Sigma\nu_i\,(\Delta_f G_i^\circ) = \Delta_f G^\circ_{\text{Product}} + y\Delta_f G^\circ_{H_2O} - x\Delta_f G^\circ_{CO_2} - n\Delta_f G_{(H^+ + e^-)}\,. \tag{13}$$

The free energy of formation (from H_2) of a proton-electron pair is, by the definition of the reversible hydrogen electrode (RHE) potential scale

$$\Delta_f G_{(H^+ + e^-)} = -\mathcal{F}U_{\text{RHE}}\,. \tag{14}$$

where $\mathcal{F}$ is Faradays constant and URHE is the potential on the RHE scale. At the standard equilibrium potential $U_{\text{RHE}} = U^\circ_{CO_2R}$, the free energy is zero, i.e. $\Delta_{CO_2R}G^\circ = 0$. We can thus solve for UCO2R:

$$U^\circ_{CO_2R} = \frac{1}{n\mathcal{F}}\left(x\Delta_f G^\circ_{CO_2} - \Delta_f G^\circ_{\text{Product}} - y\Delta_f G^\circ_{H_2O}\right)\,. \tag{15}$$

For example, the CO_2 reduction reaction to pripionaldehyde is

$$3\,CO_2 + 16\,(H^+ + e^-) \longrightarrow CH_3CH_2CHO_{(aq)} + 5\,H_2O\,. \tag{16}$$

The standard equilibrium potential for this reaction is

$$U^\circ = \frac{1}{16\mathcal{F}}\left(3\Delta_f G^\circ_{CO_2} - \Delta_f G^\circ_{CH_3CH_2CHO_{(aq)}} - 5\Delta_f G^\circ_{H_2O}\right) \tag{17}$$

$$= \frac{1}{16\cdot 96487\frac{\text{C}}{\text{mol}}}\left(3\cdot(-394.4) - (-133.3) - 5\cdot(-237.1)\right)\frac{\text{kJ}}{\text{mol}} \tag{18}$$

$$= 0.0879\,\text{V}\,, \tag{19}$$

which is rounded to 0.09 V vs RHE in Table 2. All of the standard equilibrium potentials in Table 2 are calculated from the free energies of formation of the reactants and products just like in this example. Notice the key role of the definition of the RHE potential as capturing the free energy of both electrons and protons. On the SHE scale, the potential only captures the free energy of the electrons, and the equilibrium potential depends on the free energy of the protons, i.e. the pH. This will be commented on further below.

CO reduction

As described several places in the main-text, CO is an important intermediate in CO_2 reduction to more reduced products. As such, the equilibrium potentials for CO reduction are also of interest. CO reduction reaction standard equilibrium potentials can be calculated from the free energies of formation of the reactants and products, as described above, but here we describe a shortcut for calculating the CO reduction reaction standard equilibrium potential if the CO_2 reduction reaction standard equilibrium potential is known. If the CO_2 reduction to a reaction to a product can be written

$$x\,CO_2 + n\,(H^+ + e^-) \longrightarrow \text{Product} + y\,H_2O\,, \tag{20}$$

then the CO reduction reaction to the same product can be obtained by subtracting x times the CO_2 reduction reaction to CO,

$$CO_2 + 2\,(H^+ + e^-) \longrightarrow CO + H_2O\,, \tag{21}$$

to obtain

$$x\,CO + (n-2x)\,(H^+ + e^-) \longrightarrow \text{Product} + (y-x)\,H_2O\,. \tag{22}$$

The equilibrium potential of this reaction, from the free energies of formation, is

$$U^\circ_{\mathrm{COR}} = \frac{1}{(n-2x)\mathcal{F}} \left(x\Delta_f G^\circ_{\mathrm{CO}} - \Delta_f G^\circ_{\mathrm{Product}} - (y-x)\Delta_f G^\circ_{\mathrm{H_2O}} \right) . \tag{23}$$

This can be rewritten to obtain

$$U^\circ_{\mathrm{COR}} = \frac{1}{(n-2x)\mathcal{F}} \left[\left(x\Delta_f G^\circ_{\mathrm{CO_2}} - y\Delta_f G^\circ_{\mathrm{H_2O}} - \Delta_f G^\circ_{\mathrm{Product}} \right) - x\left(\Delta_f G^\circ_{\mathrm{CO_2}} - \Delta_f G^\circ_{\mathrm{H_2O}} - \Delta_f G^\circ_{\mathrm{CO}} \right) \right] \tag{24}$$

$$= \frac{1}{(n-2x)\mathcal{F}} \left[n\mathcal{F}U^\circ_{\mathrm{CO_2R}} - x\cdot 2\mathcal{F}U^\circ_{\mathrm{CO_2R}}(\mathrm{CO}) \right] \tag{25}$$

$$= \frac{nU^\circ_{\mathrm{CO_2R}} - 2xU^\circ_{\mathrm{CO_2R}}(\mathrm{CO})}{n-2x} , \tag{26}$$

where $U^\circ_{\mathrm{CO_2R}}(\mathrm{CO}) = -0.104$ V is the standard equilibrium potential for CO2 reduction to CO. For example, the reduction of CO to propionaldehyde is

$$U^\circ_{\mathrm{COR}}(\mathrm{CH_3CH_2CHO_{(aq)}}) = \frac{16\cdot(0.0878\,\mathrm{V}) - 2\cdot 3\cdot(-0.104\,\mathrm{V})}{16-2\cdot 3} = 0.203\,\mathrm{V} \tag{27}$$

vs RHE.
Note that in the equation above, n is still the number of electrons transferred in the CO_2 reduction reaction. In terms of the number of electrons transferred in the CO reduction reaction, $n_{\mathrm{COR}} = n - 2x$, the equation reads:

$$U^\circ_{\mathrm{COR}} = \frac{(n_{\mathrm{COR}} + 2x)U^\circ_{\mathrm{CO_2R}} - 2xU^\circ_{\mathrm{CO_2R}}(\mathrm{CO})}{n_{\mathrm{COR}}} . \tag{28}$$

1.3 Energy Content of Carbon Products

The x-axis in Figure 2 gives the energy content of various carbon products. The energy content of each carbon product was calculated according to the free energies of formation in Table S1 and the stoichiometry of the carbon-recycling reaction (rxn 1 of the main text) for each product, which is the reverse of its combustion reaction. The carbon recycling reaction takes the form of

$$x\,\mathrm{CO_2} + y\,\mathrm{H_2O} \longrightarrow \mathrm{Product} + z\,\mathrm{O_2} \tag{29}$$

The carbon recycling reaction can be obtained by adding two electrochemical half-reactions: the CO_2 reduction reaction forming the product, and the oxygen evolution reaction (OER), balanced such that the electron transfers cancel. For instance, the CO_2 recycling reaction for ethanol is

$$2\,\mathrm{CO_2} + 12\,(\mathrm{H^+} + \mathrm{e^-}) \longrightarrow \mathrm{CH_3CH_2OH_{(aq)}} + 3\,\mathrm{H_2O} \tag{30}$$

$$+3\cdot[2\,\mathrm{H_2O} \longrightarrow \mathrm{O_2} + 4\,(\mathrm{H^+} + \mathrm{e^-})] \tag{31}$$

$$2\,\mathrm{CO_2} + 3\,\mathrm{H_2O} \longrightarrow \mathrm{CH_3CH_2OH_{(aq)}} + 3\,\mathrm{O_2} \tag{32}$$

The free energy change for this reaction can be calculated from the free energies of formation for ethanol, water, O_2, and CO_2 in Table S1. However, there is a shortcut. Given the equilibrium potential for CO_2 reduction, $U^\circ_{\mathrm{CO_2R}}$, to a product involving n electron transfers to x molecules of CO_2, the free energy for the carbon recycling reaction is:

$$\begin{aligned}\Delta_{\mathrm{recycling}}G^\circ(\mathrm{Product}) &= \Delta_f G^\circ(\mathrm{Product}) + z\Delta_f G^\circ(\mathrm{O_2}) - x\Delta_f G^\circ(\mathrm{CO_2}) - y\Delta_f G^\circ(\mathrm{H_2O}) \\ &= n\mathcal{F}\left(U^\circ_{\mathrm{OER}} - U^\circ_{\mathrm{CO_2R}}(\mathrm{Product})\right) \end{aligned} \tag{33}$$

Where $U^\circ_{\mathrm{OER}} = 1.23$ V vs RHE is the equilibrium potential for the oxygen-evolution reaction. For example, the energy content of ethanol is:

$$\begin{aligned}\Delta_{\mathrm{recycling}}G^\circ(\mathrm{CH_3CH_2OH_{aq}}) &= 12\mathcal{F}\left(U^\circ_{\mathrm{OER}} - U^\circ_{\mathrm{CO_2R}}(\mathrm{CH_3CH_2OH_{aq}})\right) \\ &= 12\cdot 96487\frac{\mathrm{C}}{\mathrm{mol}}(1.23\,\mathrm{V} - 0.09\,\mathrm{V}) \qquad (34) \\ &= 1320\frac{\mathrm{kJ}}{\mathrm{mol}} \qquad (35)\end{aligned}$$

All of the economic and energetic quantities in Figure 2 are normalized to mass of carbon. This is accomplished by taking the molar energy content and dividing by the mass of carbon per mol of product. Since there are x carbon atoms in the product, this means the carbon-normalized energy content, $E_\mathrm{C}(\text{Product})$, is:

$$E_\mathrm{C}(\text{Product}) = \frac{\Delta_\text{recycling} G^\circ(\text{Product})}{x M_\mathrm{C}} \tag{36}$$

where M_C is the molar mass of carbon. For ethanol, this means:

$$\begin{aligned}
E_\mathrm{C}(\mathrm{CH_3CH_2OH}) &= \frac{\Delta_\text{recycling} G^\circ(\mathrm{CH_3CH_2OH_{(aq)}})}{2 M_\mathrm{C}} && (37)\\
&= \frac{1320\,\frac{\mathrm{kJ}}{\mathrm{mol}}}{2 \cdot 12\,\frac{\mathrm{g_C}}{\mathrm{mol}}} && (38)\\
&= 55.0\,\frac{\mathrm{kJ}}{\mathrm{g_C}} \cdot \left(\frac{1\,\mathrm{MWh}}{3.6{\cdot}10^6\,\mathrm{kJ}}\right) \cdot \left(\frac{10^6\,\mathrm{g_C}}{1\,\mathrm{t_C}}\right) && (39)\\
&= 15.3\,\frac{\mathrm{MWh}}{\mathrm{t_C}} && (40)
\end{aligned}$$

The energy content for each of the other products was calculated in the same way.

1.4 pH Dependence on the RHE and SHE Scales

As mentioned above, the electrochemical potential on the RHE scale can be defined by

$$U_\mathrm{RHE} = -\frac{1}{\mathcal{F}} \Delta_f G(\mathrm{H^+} + \mathrm{e^-})\,. \tag{41}$$

The equilibrium potential for a reaction or for an elementary step is well-defined (i.e., pH-independent) on the RHE scale if the stoichiometric coefficients are identical for protons and electrons.
In contrast, the electrochemical potential on the SHE scale can be defined by

$$U_\mathrm{SHE} = -\frac{1}{\mathcal{F}} \Delta_f G(\mathrm{e^-})\,. \tag{42}$$

The equilibrium potential for a reaction or for an elementary step in which protons are consumed or produced (or equivalently, in which hydroxide is produced or consumed) depends on the free energy of protons, and thus on the pH.
The potentials on the two scales are related by

$$\begin{aligned}
U_\mathrm{RHE} &= U_\mathrm{SHE} - \frac{1}{\mathcal{F}} \Delta_f G(\mathrm{H^+}) && (43)\\
&= U_\mathrm{SHE} - \frac{RT}{\mathcal{F}} \ln\left(a(\mathrm{H^+})\right) && (44)\\
&= U_\mathrm{SHE} + \frac{RT\ln(10)}{\mathcal{F}} \mathrm{pH} && (45)\\
&= U_\mathrm{SHE} + 59\,\mathrm{mV} \cdot \mathrm{pH}\,, && (46)
\end{aligned}$$

where we've used the fact that the free energy of protons in their standard state (an idealized 1 M solution) is defined to be zero, and the definition $\mathrm{pH} = -\log(a(\mathrm{H^+}))$. 59 mV $= \frac{RT\ln(10)}{\mathcal{F}}$ is the Nernst constant at room temperature.
Since the equilibrium potential for a $\mathrm{CO_2}$ reduction reaction ($U^\circ_\mathrm{CO_2R}$) with equal numbers of protons and electrons transferred is pH-independent on the RHE scale, it decreases with increasing pH on the SHE scale:

$$U_\mathrm{SHE,\,CO_2R} = U^\circ_\mathrm{CO_2R} - \frac{RT\ln(10)}{\mathcal{F}} \mathrm{pH}, \tag{47}$$

Deprotonated Products

If the number of protons does not equal the number of electrons transferred, as is the case when the product of CO_2 reduction is the conjugate base of an organic acid such as formate or acetate, then the equilibrium potential is in general pH-dependent on both scales. The free energy change for the CO_2 reduction reaction to the base A^- is the sum of the free energy change of the CO_2 reduction reaction to the acid HA plus the free energy change of the deprotonation step.

$$\Delta G_{\mathrm{CO_2R}}(\mathrm{A^-}) = \Delta G_{\mathrm{CO_2R}}(\mathrm{HA}) + \Delta G(\mathrm{HA} \longrightarrow \mathrm{H^+} + \mathrm{A^-}) \tag{48}$$

The standard free energy for the deprotonation reaction is related to the pKa of HA:

$$\Delta G^\circ(\mathrm{HA} \longrightarrow \mathrm{H^+} + \mathrm{A^-}) = -RT\ln(K_a) = RT\ln(10)\mathrm{pKa} \tag{49}$$

Assuming that CO_2, H_2O, and A^- are in their thermodynamic standard states (but not protons or electrons), this is

$$\Delta G^\circ(\mathrm{HA} \longrightarrow \mathrm{A^-}) = -RT\ln\left(\frac{K_a}{a(\mathrm{H^+})}\right) = RT\ln(10)(\mathrm{pKa} - \mathrm{pH}) \tag{50}$$

and substituting Equation 50 into Equation 48, this gives

$$\Delta G^\circ_{\mathrm{CO_2R}}(\mathrm{A^-}) = \Delta G^\circ_{\mathrm{CO_2R}}(\mathrm{HA}) + RT\ln(10)(\mathrm{pKa} - \mathrm{pH}) \tag{51}$$

$$= n\mathcal{F}U^\circ_{\mathrm{CO_2R}}(\mathrm{HA}) + RT\ln(10)(\mathrm{pKa} - \mathrm{pH})\,. \tag{52}$$

Dividing both sides by $n\mathcal{F}$ gives

$$U^\circ_{\mathrm{CO_2R}}(\mathrm{A^-}) = U^\circ_{\mathrm{CO_2R}}(\mathrm{HA}) + \frac{RT\ln(10)}{n\mathcal{F}}(\mathrm{pH} - \mathrm{pKa})\,. \tag{53}$$

This gives the pH-dependence of CO_2 reduction to a deprotonated product on the RHE scale. By Equation 47, the equilibrium potential CO_2 reduction to A^- is

$$U\mathrm{SHE}, \mathrm{CO_2R}(\mathrm{A^-}) = U^\circ_{\mathrm{CO_2R}}(\mathrm{HA}) - \frac{RT\ln(10)}{n\mathcal{F}}\left((n-1)\mathrm{pH} + \mathrm{pKa}\right)\,. \tag{54}$$

For instance, the equilibrium potential of CO_2 reduction to formate ($HCOO^-$) at pH=6.8 (0.1 M CO_2-saturated potassium bicarbonate) is

$$U^\circ_{\mathrm{CO_2R}}(\mathrm{HCOO^-}) = U^\circ_{\mathrm{CO_2R}}(\mathrm{HCOOH}) + \frac{RT\ln(10)}{2\mathcal{F}}(\mathrm{pH} - \mathrm{pKa}(\mathrm{HCOOH}))\,. \tag{55}$$

$$= -0.115\,\mathrm{V} + \frac{59\,\mathrm{mV}}{2}(6.8 - 3.77) \tag{56}$$

$$= -0.025\,\mathrm{V} \tag{57}$$

vs RHE, or

$$U^\circ_{\mathrm{CO_2R}}(\mathrm{HCOO^-}) = U^\circ_{\mathrm{CO_2R}}(\mathrm{HCOOH}) - \frac{RT\ln(10)}{2\mathcal{F}}((2-1)\mathrm{pH} + \mathrm{pKa}(\mathrm{HCOOH}))\,. \tag{58}$$

$$= -0.115\,\mathrm{V} - \frac{59\,\mathrm{mV}}{2}(6.8 + 3.77) \tag{59}$$

$$= -0.426\,\mathrm{V} \tag{60}$$

vs SHE.

Hori's Relationships

As discussed in Section 3.3.1 Hori used buffer solutions spanning a bulk pH range of 6 to 12 to study CO reduction on Cu as a function of pH[1]. He reports his results on the SHE scale, and the pH dependence on the RHE scale is not trivial to extract from his reported results.

Hori et al. treated their observations in the framework of decoupled electron transfers, and explained the pH dependence of the potential on an SHE scale needed to reach a given CH_4 partial current density in terms of the Tafel equation with an exchange current density proportional to proton concentration. The Tafel equation is

$$J_{\mathrm{CH_4}} = A \exp\left(-\alpha_{\mathrm{CH_4}} \frac{\mathcal{F}}{RT}(U_{\mathrm{SHE}} - U^{\circ}_{\mathrm{SHE}})\right), \tag{61}$$

or, in logarithmic form,

$$\log(J_{\mathrm{CH_4}}) = -\alpha_{\mathrm{CH_4}} \frac{\mathcal{F}}{RT\log(10)}(U_{\mathrm{SHE}} - U^{\circ}_{\mathrm{SHE}}) + \log(A)\,. \tag{62}$$

While ethylene fits this relationship regardless of pH, methane only fits it if the pre-exponential factor A was taken to be proportional to the proton concentration, i.e.,

$$A = Ba(\mathrm{H}^+)\,. \tag{63}$$

Making this substitution, and using the definition of pH, they arrive at

$$\log(J_{\mathrm{CH_4}}) + \mathrm{pH} = -\alpha_{\mathrm{CH_4}} \frac{\mathcal{F}}{RT\log(10)}(U_{\mathrm{SHE}} - U^{\circ}_{\mathrm{SHE}}) + \log(B)\,. \tag{64}$$

The left side of this equation, $\log(J_{\mathrm{CH_4}}) + \mathrm{pH}$, is the y-axis in Figure 9, taken from Hori et al[1].

To convert this to a pH-dependence of methane production in mV per pH unit, we set $J_{\mathrm{CH_4}}$ to a fixed value, J_1, and solve for U:

$$U_{\mathrm{SHE}} = U^{\circ}_{\mathrm{SHE}} + \frac{1}{\alpha_{\mathrm{CH_4}}}\frac{RT\log(10)}{\mathcal{F}}\left(\log(B) - \log(J_1) - pH\right),. \tag{65}$$

Hori fit the data to $\alpha_{\mathrm{CH_4}} = 1.33$. Plugging this in gives

$$\begin{aligned} U_{\mathrm{SHE}} &= U^{\circ}_{\mathrm{SHE}} + \frac{1}{1.33}(59\,\mathrm{mV})\left(\log(B) - \log(J_1) - pH\right) && (66)\\ &= ... + 59\,\mathrm{mV}\left(-\frac{1}{1.33}\right)\mathrm{pH} && (67)\\ &= ... - 44.4\,\mathrm{mV}\cdot\mathrm{pH}\,, && (68)\end{aligned}$$

i.e, for each increase of one pH unit, a potential more cathodic on the SHE scale by ≈ 45 mV is required to reach the same partial current density for CO_2 reduction to CH_4.

Converting this to the RHE via Equation 46 gives

$$\begin{aligned} U_{\mathrm{RHE}} &= U^{\circ}_{\mathrm{SHE}} + \frac{1}{\alpha_{\mathrm{CH_4}}}\frac{RT\log(10)}{\mathcal{F}}\left(\log(B) - \log(J_1)\right) + \frac{RT\log(10)}{\mathcal{F}}\left(1 - \frac{1}{\alpha_{\mathrm{CH_4}}}\right)\mathrm{pH} && (69)\\ &= ... + 59\,\mathrm{mV}\left(1 - \frac{1}{1.33}\right)\mathrm{pH} && (70)\\ &= ... + 14.6\,\mathrm{mV}\cdot\mathrm{pH},, && (71)\end{aligned}$$

i.e, for each increase of one pH unit, the potential can move anodic by ≈ 15 mV on the RHE scale and maintain the same partial current density for CO_2 reduction to CH_4.

2 Economics: Raw Data and Calculations

This section describes the data, calculations, and assumptions used in the bottom section of Table 1 and in Figure 2.

2.1 Global Non-Energy Carbon in Industry

The bottom portion of Table 1 lists five major non-energy carbon sources/sinks in industry: cement, steel, plastic, ammonia, and aluminum, and gives the amount of carbon involved in each of those industries in GtC/year. These values were obtained as follows:

Cement
From US Geological Survey, Cement. url:
`https://minerals.usgs.gov/minerals/pubs/commodity/cement/mcs-2018-cemen.pdf` Annual production is 4,100,000 thousand metric tons in 2017, or 4.1 Gt/yr. Cement is 2/3 CaO by weight. Cement is produced from calcium carbonate in the calcination process, and one molecule of CO_2 is released per unit of CaO, according to

$$\mathrm{CaCO_3} \longrightarrow \mathrm{CaO} + \mathrm{CO_2} \tag{72}$$

The total mass of carbon emissions due to cement calcination is thus

$$w_{\text{C, cement}} = \frac{2}{3} \cdot \frac{M_{\mathrm{C}}}{M_{\mathrm{CaO}}} \cdot 4.1\,\frac{\mathrm{Gt}}{\mathrm{yr}} = 590\,\frac{\mathrm{MtC}}{\mathrm{yr}} \tag{73}$$

where M_{C} and M_{CaO} are the molar masses of carbon and CaO, respectively.

Steel
From World Steel in Figures 2018, World Steel Association. URL:
`https://www.worldsteel.org/en/dam/jcr:`
`f9359dff-9546-4d6b-bed0-996201185b12/World\%2520Steel\%2520in\%2520Figures\%25202018.pdf`
gives the value 1689 Mton/year in 2017. However, this presumably includes recycled steel, so instead, we consider the value for pig iron, which is produced first from iron ore. The value for pig iron is 1167 Mton/year in 2017. Pig iron is produce in blast furnaces by a reaction between coke, air, and iron ore. The coke is converted to CO, which reduces the iron ore (approximately Fe_2O_3).

$$\mathrm{C} + \frac{1}{2}\,\mathrm{O_2} \longrightarrow \mathrm{CO} \tag{74}$$

$$\mathrm{Fe_2O_3} + 3\,\mathrm{CO} \longrightarrow 2\,\mathrm{Fe} + 3\,\mathrm{CO_2} \tag{75}$$

Combined, the overall stoichiometry is

$$2\,\mathrm{Fe_2O_3} + 6\,\mathrm{C} + 3\,\mathrm{O_2} \longrightarrow 4\,\mathrm{Fe} + 6\,\mathrm{CO_2} \tag{76}$$

Thus, there are 6 atoms of carbon released for every 4 atoms of metallic iron in steel. As an approximation, we consider the total mass of pig iron to be pure iron. The yearly mass of carbon in pig iron production, and thus production of new steel, is thus

$$w_{\text{C, steel}} = \frac{6}{4} \cdot \frac{M_{\mathrm{C}}}{M_{\mathrm{Fe}}} \cdot 1167\,\frac{\mathrm{Gt}}{\mathrm{yr}} = 380\,\frac{\mathrm{MtC}}{\mathrm{yr}} \tag{77}$$

where M_{C} and M_{Fe} are the molar masses of carbon and iron, respectively.

Plastic
From Geyer et al, "Production, use, and fate of all plastics ever made" Science Advances, 2017. In this article, estimates are given for the year 2015 for the mass of the pool of all plastic in use and all plastic accumulated in landfills and the environment, as well as the yearly fluxes including new plastic production, recycling, and discarding. We calculate the carbon content of the discarded plastic, estimating an average molecular formula of $(CH_2)_n$. This may overestimate the carbon content, as e.g., polycarbonates are a smaller portion carbon by mass, but not by much since polyethylene and polypropelyne, which approximately follow that formula, make up the majority of all plastic discarded in 2015. From the article: "We estimate that in 2015... 302 Mt left [the use phase]" The carbon content, assuming the $(CH_2)_n$ formula, of 302/yr Mt plastic is

$$w_{\text{C, plastic}} = \frac{M_{\mathrm{C}}}{M_{\mathrm{CH_2}}} \cdot 302\,\frac{\mathrm{Gt}}{\mathrm{yr}} = 260\,\frac{\mathrm{MtC}}{\mathrm{yr}} \tag{78}$$

Ammonia
Ammonia is produced in vast quantities as the precursor to synthetic fertilizers, necessary to sustain the worlds population. From the US Geological Survey, fixed Nitrogen, url: `https://minerals.usgs.gov/minerals/pubs/commodity/nitrogen/mcs-2017-nitro.pdf` we get the amount 140,000 thousand metric of fixed nitrogen in 2016. Nitrogen is formed by the Habor Bosch process by reaction with hydrogen:

$$\mathrm{N_2 + 3\,H_2 \longrightarrow 2\,NH_3}\,, \tag{79}$$

, where the hydrogen is produced by steam reforming of methane:

$$\mathrm{CH_4 + H_2O \longrightarrow CO + 3\,H_2}\,, \tag{80}$$

and the water-gas shift to remove the CO,

$$\mathrm{CO + H_2O \longrightarrow CO_2 + H_2}\,. \tag{81}$$

Combining the three above reactions gives the following overall process:

$$\mathrm{3\,CH_4 + 6\,H_2O + 4\,N_2 \longrightarrow 8\,NH_3 + 3\,CO_2}\,, \tag{82}$$

and so three molecules of CO_2 are produced in the oxidation process that ultimately balances the reduction of four molecules of N_2 to ammonia. The total mass of carbon used in ammonia production is thus:

$$\frac{3}{4}\frac{M_{\mathrm{C}}}{M_{\mathrm{N_2}}}\cdot 140\frac{\mathrm{Mt}}{\mathrm{yr}} = 45\frac{\mathrm{MtC}}{\mathrm{yr}}\,. \tag{83}$$

Aluminum
From US Geological Survey, Aluminum. url: `https://minerals.usgs.gov/minerals/pubs/commodity/aluminum/mcs-2017-alumi.pdf` States world production as 576,000 thousand metric tons of aluminum in 2016. Aluminum is produced from alumina ore electrochemically by the HallHeroult process. This involves a carbon cathode on which molten aluminum is deposited from a molten electrolyte consisting of Al_2O_3, AlF_3, and NaF, and a sacrificial carbon anode which is oxidized primarily CO_2 in the process. The overall reaction is approximately:

$$\mathrm{2\,Al_2O_3 + 3\,C \longrightarrow 4\,Al + 3\,CO_2} \tag{84}$$

The carbon consumed for the 2016 world aluminum process was, according to this stoichiometry:

$$\frac{3}{4}\frac{M_{\mathrm{C}}}{M_{\mathrm{Al}}}\cdot 57.6\frac{\mathrm{Mt}}{\mathrm{yr}} = 19.2\frac{\mathrm{MtC}}{\mathrm{yr}}\,. \tag{85}$$

2.2 Economics of CO_2 Reduction Products

This section of the Supplementary Information describes the economic raw data and calculations for each carbon product used in Figure 2, in order of decreasing global carbon-normalized production. We took a number of economic values from the techno-economic analysis by Jouny et al[2], for which the authors average values taken from various market resources, and we found others elsewhere as described below.

Coal
The energy content of coal was approximated as that for carbon in its standard state, graphite. The energy content is 394 kJ/mol or 9.1 MWh/tC. Coal is the carbon product with the largest global production by mass of carbon. The International Energy Agency (Market Report Series: Coal 2017, url: https://www.iea.org/coal2017/) states that the global demand of coal in 2016 was 5,357 Mt. Approximating that coal is 100% carbon by weight, this is 5.375 GtC. The price of coal was taken from Business Insiders Commodity prices (url: https://markets.businessinsider.com/commodities/coal-price) on November 21, 2018, as USD $77 per ton. Again assuming coal is 100% carbon by weight, this is 77 USD/tC.

Natural Gas
The energy content of natural gas was approximated as that for methane. The energy content is 818 kJ/mol or 18.9 MWh/tC. The global market in 2016 was Vgas = 3630 billion cubic meters according to the International Energy Agency (Market Report Series: Gas 2016, Press Release, url: `https://www.iea.org/newsroom/news/2017/july/iea-sees-global-gas-demand-rising-to-2022-as-us-drives-market-transformation.html`). To convert this to mass of natural gass, mgas, we multiply by the density of methane as given by the ideal gas law at 1 bar at 25 C.

$$\dot{m}_{\mathrm{NG}} = \dot{v}_{\mathrm{NG}} \cdot \frac{p^\circ M_{\mathrm{CH_4}}}{RT^\circ} = 3.63{\cdot}10^{12}\,\frac{\mathrm{m}^3}{\mathrm{yr}} \cdot \frac{1\,\mathrm{bar} \cdot 16.0\,\frac{\mathrm{g}}{\mathrm{mol}}}{8.315\,\frac{\mathrm{J}}{\mathrm{mol{\cdot}K}} \cdot 298.15\,\mathrm{K}} = 2.35\,\frac{\mathrm{Gt}}{\mathrm{yr}} \tag{86}$$

The mass of the carbon content of the natural gas is obtained by adjusting for the carbon content of methane.

$$\dot{m}_{\mathrm{C,NG}} = \dot{m}_{\mathrm{NG}} \frac{M_{\mathrm{C}}}{M_{\mathrm{CH_4}}} = 1.76\,\frac{\mathrm{GtC}}{\mathrm{yr}} \tag{87}$$

The price of Natural Gas was obtained from Business Insiders Commodity prices (url: `https://markets.businessinsider.com/commodities/natural-gas-price`) on November 21, 2018, as USD $4.75 per million British thermal units (MBTU). This was converted to a price per ton according to

$$p_{\mathrm{NG}} = 4.75\,\frac{\mathrm{USD}}{\mathrm{MBTU}} \cdot \left(\frac{1\,\mathrm{MBTU}}{1.055{\cdot}10^6\,\mathrm{kJ}}\right) \cdot 818\,\frac{\mathrm{kJ}}{\mathrm{mol}} \cdot \frac{1}{16.0\frac{\mathrm{g}}{\mathrm{mol}}} \cdot \left(\frac{1{\cdot}10^6\,\mathrm{g}}{1\,\mathrm{t}}\right) = 221\,\frac{\mathrm{USD}}{\mathrm{t}}\,, \tag{88}$$

and to a price per ton of carbon according to

$$p_{\mathrm{C,NG}} = p_{\mathrm{NG}} \frac{M_{\mathrm{CH_4}}}{M_{\mathrm{C}}} = 295\,\frac{\mathrm{USD}}{\mathrm{tC}}\,. \tag{89}$$

Ethylene
The energy content of ethylene, calculated as described, is 1330 kJ/mol, or 15.4 MWh/tC. The global market size and price are taken from Jouny et al[2] as 140 Mt/yr and 1.3 USD/kg. This corresponds to 120 MtC/yr and 1520 USD/tC.

CO, Syngas
CO was considered in its standard pure state for the energy content. COs energy content, calculated as described, is 257 kJ/mol, or 5.95 MWh/tC. The world market size and price of CO in syngas were taken from Jouny et al[2] as 150 Mt/yr and 0.06 USD/kg, respectively. This corresponds to 64 MtC/yr and 140 USD/tC, respectively.

Methanol
The energy content of methanol, calculated as described, is 726 kJ/mol, or 16.8 MWh/tC. The size of the global market was taken from Jouny et al[2] to be 110 Mt/yr, corresponding to 41 MtC/yr. We estimated the current market price by averaging the most recent (October, 2018) prices for Europe, North America, and Asia Pacific posted by Methanex (url: https://www.methanex.com/our-business/pricing). This was 486 USD for a ton of methanol, corresponding to 1300 USD/tC.

Ethanol
The energy content of ethanol, calculated as described, is 1320 kJ/mol, or 15.2 MWh/tC. The global market size and price are taken from Jouny et al[2] as 77 Mt/yr and 1.00 USD/kg. This corresponds to 40.1 MtC/yr and 1920 USD/tC.

CO, Pure
We again used the energy content of CO in its standard state: 257 kJ/mol, or 5.95 MWh/tC. The largest demand for pure CO is for producing phosgene, COCl2, which is in turn used for production of polycarbonate plastics among other things. The size of the global phosgene market was 8.526 kilotons in 2015 according to "Global Phosgene Outlook 2016-202" from Market Research Store (url: https://www.marketresearchstore.com/report/global-phosgene-outlook-2016-2021-98559). By adjusting for

the ratio of molar masses ($M_{\mathrm{COCl_2}} = 98.9$ g/mol), this corresponds to 2.41 Mt of CO per year, or a carbon flux of 1.04 MtC/yr. Pure CO from CO_2 could become a much larger market if future steel production were to use CO directly as the reductant, rather than producing CO from coke. The market price of pure CO was taken from Jouny et al[2] as 0.6 USD/kg, which corresponds to 1400 USD/tC.

Acetaldehyde
The energy content of acetaldehyde is 1120 kJ/mol, or 13.0 MWh/tC. The global market size was predicted by Global Industry Analysts Inc, in 2008, to be 1.26 Mt in 2012 (published on PRWeb, url: `http://www.prweb.com/releases/acetaldehyde/acetic_acid/prweb1553564.htm`). This corresponds to 0.68 MtC/yr. The price of acetaldehyde was accessed on ICIS Indicative Chemical Prices (url: `https://www.icis.com/explore/commodities/chemicals/channel-info-chemicals-a-z/`) to be 0.456 USD/lb, or 1000 USD/t. This corresponds to 1830 USD/tC.

Formic Acid
The energy content of formic acid is 259 kJ/mol, or 6.0 MWh/tC. The global market size and price are taken from Jouny et al[2] as 0.6 Mt/yr and 0.74 USD/kg. This corresponds to 0.16 MtC/yr and 2840 USD/tC.

Propanol
The energy content of formic acid is 1960 kJ/mol, or 15.1 MWh/tC. The global market size and price are taken from Jouny et al[2] as 0.2 Mt/yr and 1.43 USD/kg. This corresponds to 0.12 MtC/yr and 2380 USD/tC.

3. Computational Studies: Energetics and Kinetics of Elementary Steps

Table S2: Calculated barriers for CO_2R to CO via various methods. Identical barriers calculated using different methods are highlighted by the same color.

Group	**# water molecules**	**transition state search method**	**potential dependence**	**reaction step**	**facet**	**pH**	**potential (vs RHE)**	**barrier (eV)**	**β**	**Ref**
Janik	1 to 2	H shuttling	H shuttling	$CO_{2(g)} \rightarrow COOH$	111	-	0	0.87	–0.44	[3,4]
				$COOH \rightarrow CO$	111	-	0	0.80	–0.52	
				$CO_{2(g)} \rightarrow COOH$	111	-	0	0.74	–0.53	[4]
				$CO_{2(g)} \rightarrow COOH$	100	-	0	1.19	–0.43	[5]
				$COOH \rightarrow CO$	100	-	0	0.92	–0.44	
Goddard	48	metadynamics	charge extrapolation	$CO_{2(g)} \rightarrow CO_2$	100	7	-0.4	0.43	-	[6]
				$CO_2 \rightarrow COOH$	100	7	-0.4	0.37	-	
				$COOH \rightarrow CO$	100	7	-0.4	0.30	-	
Nørskov	5 (1 layer)	NEB	charge extrapolation	$CO_2 \rightarrow COOH$	211	7	0	0.21	–0.5	[7]
				$COOH \rightarrow CO$				0.67	–0.5	

Table S3: Calculated barriers for CO reduction to C_1 products via various methods. Identical barriers calculated using different methods are highlighted by the same color.

Group	# water molecules	transition state search method	potential dependence	reaction step	facet	pH	potential (*vs.* RHE)	electrochemical barrier (eV)	β	surface hydrogenation barrier (eV)	Ref
Jin	0	NEB	-	CO→CHO	100	-	-	-	-	2.43	8
				CO→COH	100	-	-	-	-	2.36	
				CO→CHO	111	-	-	-	-	1.0	
				CO→COH	111	-	-	-	-	2.6	
Head-Gordon	0 to 2	dimer method	implicit solvent	CO→CHO	100	7	0	1.35	-0.78	-	9
Goddard	1 to 2	H shuttling[#]	implicit solvent	CO→CHO	111	1	0	-	0.02	0.9	10
						7				1.29	
						12				1.62	
				CO→COH	111	1	0	**0.76***	–0.05*	**-**	
						7		**1.13***			
						12		1.44*			
				COH→CHOH	111	1	0	-	0.02	**0.55**	
						7		-		**0.9**	
						12		-		1.19	
	49	metadynamics	charge extrapolation	CO→CHO	100	-	-	-	-	**0.55**	11
				CO→COH	100	0	–0.4	0.74	-	1.45	
	48			CO→CHO	100	7	–0.59	**0.97**	-	**0.96****	12
				CO→COH	100	7	–0.59	1.21	-	-	

(Table S3 continues on next page)

Janik & Asthagiri	1 to 2	H shuttling	H shuttling	CO→CHO	111	-	0	1.18	-0.51***	**0.98**	[3,4]
				CO→COH	111	-	0	**0.73**	–0.45	-	
				COH→C	111	-	0	**1.10**	–0.58	-	
				CO→CHO	100	-	0	-	–0.53	0.64	[5]
				CO→COH	100	-	0	**0.92**	–0.46	-	
				COH→C	100	-	0	**1.00**	–0.46	-	
Nørskov	5 (1 layer)	NEB	charge extrapolation	CO→CHO	111	7	0	**1.34**	–0.50	1.11	[7]
				CO→COH	111	7	0	1.21	–0.50	2.35	
				COH→CHOH	111	7	0	1.65	–0.50	-	
				CO→CHO	100	7	0	**1.26**	–0.50	-	

[#] whether the H transfers through water or directly was not reported in this work; we postulate that COH is formed from transfer through H_2O as determined in Ref. [5] and have classified it as an electrochemical barrier; the reported potential dependence in ΔG however does not appear consistent with the transfer of a single electron, which may be an artefact of the assumptions applied in the model of the electrochemical interface (*i.e.*, $\beta = -1$)

*these values correspond to ΔG as it was reported to be higher than the activation energy

**1.01 eV for H* + $CO_{(g)}$

***β here was reported for the surface hydrogenation process

Table S4: Calculated barriers for C-C coupling via various methods. Identical barriers calculated using different methods are highlighted by the same color.

Group	# water molecules	transition state search method	potential dependence	reaction step	facet	pH	potential (*vs.* RHE)	barrier (eV)	β*	Ref
Jin	0	NEB	-	2CO→OCCO	100	-	-	1.26	-	8
Koper	0	-	bader charge of adsorbates			-	-	1.19	–0.68	13
Head-Gordon	0 to 2	dimer method	implicit solvent			7	0	**0.53**	–0.17	9
				CO+CHO→OCCHO	100	7	0	**0.63**	–0.08	
		dimer method		OCCHO+H→OHCCHO	100	7	–1	0.58	0.5	14
		NEB					0	1.00		
		dimer method		OCCHO+H→OCCHOH			–1	0.49		
		NEB					0	0.78		
Goddard	1 to 2	H shuttling	implicit solvent	2CO→OCCO	111	1	0	1.15	0.05	10
						7		1.14		
						12		**1.14**		
	48	metadynamics	charge extrapolation	2CO→OCCO	100	7	–0.59	0.69	-	12
Janik	1 to 2	H shuttling	H shuttling			-	-	1.22**	-	5
				CO+CHO→OCCHO	100	-	-	0.77	-	
				2CO→OCCO	111	-	-	1.7	-	
Nørskov	5 (1 layer)	NEB	charge extrapolation	2CO→OCCO	100	-	-	0.45	-	15
				2CO→OCCO	111	-	-	0.72	-	
				2CO→OCCO	211	-	-	0.72	-	

*β here were reported for the C-C coupling processes

**this barrier goes down to 1.06 when 2 waters are included

4. Tabulated Data for Activity Comparison Figures

Please Note: unless directly tabulated, this data was obtained via web digitization of figures from the original manuscripts. Thus, please excuse any slight inaccuracies this may have introduced.

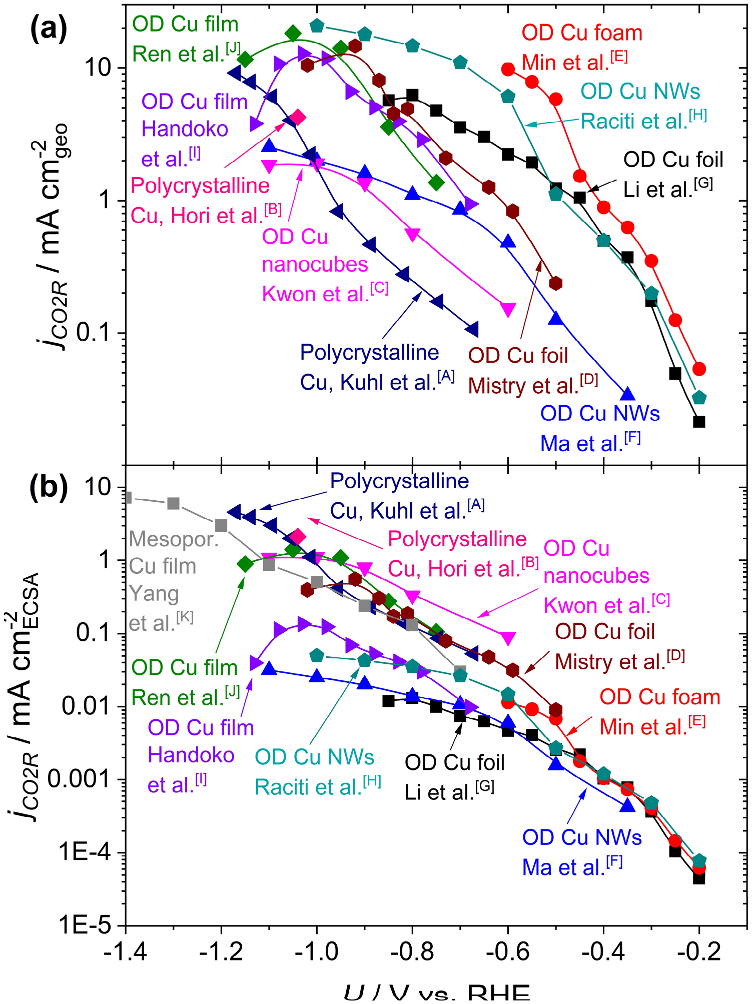

Figure 29: Comparison of CO_2R activity for various nanostructured Cu electrocatalysts with polycrystalline Cu. **(a)** CO_2R partial current density normalized to geometric surface area. **(b)** CO_2R partial current density normalized to electrochemical surface area (ECSA). The data were obtained from the following studies: [A] Kuhl *et al.*[16]; [B] Hori *et al.*[17]; [C] Kwon *et al.*[18]; [D] Mistry *et al.*[19]; [E] Min *et al.*[20]; [F] Ma *et al.*[21,22]; [G] Li *et al.*[23]; [H] Raciti *et al.*[24]; [I] Handoko *et al.*[25]; [J] Ren *et al.*[26]; [K] Yang *et al.*[27]. Studies [A,B] are polycrystalline Cu, [C-J] are oxide-derived, nanostructured Cu and [K] is non-oxide-derived nanostructured Cu.

Table S5: Tabulated Data for Figure 29, Comparison of CO_2R activity for various nanostructured Cu electrocatalysts with polycrystalline Cu

	1st Author *et al.*[ref]	**Catalyst**	**V *vs.* RHE**	**J_{CO2R} GEO (mA/cm^2)**	**J_{CO2R} ECSA (mA/cm^2)**	**Notes** *(Figure/Table references noted here refer to those within the article from which the data was obtained)*
[A]	Kuhl *et al.*[16]	Cu foil	-0.67	0.107	0.054	Geometric partial current densities (PCDs) for $>2e^-$ products obtained from Figure 6. Roughness factor (RF) ≈ 2 (from SI)
[A]	Kuhl *et al.*[16]	Cu foil	-0.75	0.172	0.086	
[A]	Kuhl *et al.*[16]	Cu foil	-0.82	0.277	0.139	
[A]	Kuhl *et al.*[16]	Cu foil	-0.89	0.464	0.232	
[A]	Kuhl *et al.*[16]	Cu foil	-0.96	0.829	0.415	
[A]	Kuhl *et al.*[16]	Cu foil	-1.01	2.229	1.115	
[A]	Kuhl *et al.*[16]	Cu foil	-1.05	4.025	2.013	
[A]	Kuhl *et al.*[16]	Cu foil	-1.09	6.077	3.039	
[A]	Kuhl *et al.*[16]	Cu foil	-1.14	7.862	3.931	
[A]	Kuhl *et al.*[16]	Cu foil	-1.17	9.177	4.589	
[B]	Hori *et al.*[17]	Cu foil	-1.04	4.250	2.125	Faradaic efficiencies and geometric current density obtained from Table 1. Assuming RF ≈ 2, based on Kuhl et al.,[16] since these two studies used similar pre-treatment procedures.
[C]	Kwon et al.[18]	OD-Cu nanocubes	-0.60	0.153	0.090	Data from KF cycled Cu foil. Faradaic efficiencies and total geometric current density obtained from Table S4 (Supporting Information). RF = 1.7, estimated from double layer capacitance obtained from CVs (Table S2).
[C]	Kwon et al.[18]	OD-Cu nanocubes	-0.80	0.565	0.332	
[C]	Kwon et al.[18]	OD-Cu nanocubes	-0.90	1.356	0.798	
[C]	Kwon et al.[18]	OD-Cu nanocubes	-1.00	1.913	1.126	
[C]	Kwon et al.[18]	OD-Cu nanocubes	-1.10	1.863	1.096	
[D]	Mistry et al.[19]	OD-Cu foil	-0.50	0.238	0.009	Data from Cu foil treated with a 20 W O_2 plasma for 2 min.
[D]	Mistry et al.[19]	OD-Cu foil	-0.59	0.830	0.031	
[D]	Mistry et al.[19]	OD-Cu foil	-0.64	1.261	0.048	
[D]	Mistry et al.[19]	OD-Cu foil	-0.73	2.095	0.079	

[D]	Mistry et al.[19]	OD-Cu foil	-0.81	4.928	0.187	Total geometric current density obtained from Figure 4, and Faradaic efficiencies obtained from Figure 5. RF = 26.4, estimated from double layer capacitance obtained from CVs (Figure S7 and Table S3, Supporting Information).
[D]	Mistry et al.[19]	OD-Cu foil	-0.84	4.538	0.172	
[D]	Mistry et al.[19]	OD-Cu foil	-0.87	8.076	0.306	
[D]	Mistry et al.[19]	OD-Cu foil	-0.92	14.726	0.558	
[D]	Mistry et al.[19]	OD-Cu foil	-1.02	10.507	0.398	
[E]	Min et al.[20]	OD-Cu foam	-0.20	0.053	6.22×10^{-5}	Data from commercial Cu foam oxidized in air at 500 °C for 2 h and reduced and reduced at -0.45 V vs. RHE. Total geometric current density and Faradaic efficiencies obtained from Figure 4a and 4b, respectively. RF = 855, estimated from double layer capacitance obtained from CVs (Figure 3c).
[E]	Min et al.[20]	OD-Cu foam	-0.25	0.125	1.46×10^{-4}	
[E]	Min et al.[20]	OD-Cu foam	-0.30	0.350	4.09×10^{-4}	
[E]	Min et al.[20]	OD-Cu foam	-0.35	0.627	7.34×10^{-4}	
[E]	Min et al.[20]	OD-Cu foam	-0.40	0.891	1.04×10^{-3}	
[E]	Min et al.[20]	OD-Cu foam	-0.45	1.530	1.79×10^{-3}	
[E]	Min et al.[20]	OD-Cu foam	-0.50	5.834	6.82×10^{-3}	
[E]	Min et al.[20]	OD-Cu foam	-0.55	7.868	9.20×10^{-3}	
[E]	Min et al.[20]	OD-Cu foam	-0.60	9.774	1.14×10^{-2}	
[F]	Ma et al.[21]	OD-Cu nanowires	-0.35	0.034	4.20×10^{-4}	Note: These data were taken from two different studies on the same material. Thus, they have been merged into a single dataset. For Ref. 22, data for 8.1 μm nanowires were used. Total geometric current densities were obtained from Figure 4 and Y, for Ref. 21 and 22, respectively. Faradaic efficiencies were obtained from Figure 5 and 4, for Ref. 21 and 22, respectively. RF = 80, estimated from double layer capacitance obtained from CVs (Figures S6 and S7 in Ref. 21; same RF assumed for Ref. 22 since it is the same material).
[F]	Ma et al.[21]	OD-Cu nanowires	-0.50	0.125	1.57×10^{-3}	
[F]	Ma et al.[21]	OD-Cu nanowires	-0.60	0.480	6.00×10^{-3}	
[F]	Ma et al.[22]	OD-Cu nanowires	-0.70	0.856	1.07×10^{-2}	
[F]	Ma et al.[22]	OD-Cu nanowires	-0.80	1.103	1.38×10^{-2}	
[F]	Ma et al.[22]	OD-Cu nanowires	-0.90	1.602	2.00×10^{-2}	
[F]	Ma et al.[22]	OD-Cu nanowires	-1.00	1.996	2.50×10^{-2}	
[F]	Ma et al.[22]	OD-Cu nanowires	-1.10	2.534	3.17×10^{-2}	
[G]	Li et al.[23]	OD-Cu foil	-0.20	0.021	4.45×10^{-5}	Data from Cu foil calcined in air at 500 °C for 12 hours.
[G]	Li et al.[23]	OD-Cu foil	-0.25	0.049	1.03×10^{-4}	

[G]	Li et al.[23]	OD-Cu foil	-0.30	0.173	3.62×10^{-4}	Total geometric current densities and Faradaic efficiencies obtained from Figure 3. RF = 480, estimated from double layer capacitance obtained from CVs (Figure S5 and Table S2, Supporting Information).
[G]	Li et al.[23]	OD-Cu foil	-0.35	0.371	7.75×10^{-4}	
[G]	Li et al.[23]	OD-Cu foil	-0.40	0.493	1.03×10^{-3}	
[G]	Li et al.[23]	OD-Cu foil	-0.45	1.051	2.19×10^{-3}	
[G]	Li et al.[23]	OD-Cu foil	-0.50	1.226	2.56×10^{-3}	
[G]	Li et al.[23]	OD-Cu foil	-0.55	1.942	4.05×10^{-3}	
[G]	Li et al.[23]	OD-Cu foil	-0.60	2.232	4.66×10^{-3}	
[G]	Li et al.[23]	OD-Cu foil	-0.65	3.012	6.29×10^{-3}	
[G]	Li et al.[23]	OD-Cu foil	-0.70	3.567	7.45×10^{-3}	
[G]	Li et al.[23]	OD-Cu foil	-0.75	4.782	9.98×10^{-3}	
[G]	Li et al.[23]	OD-Cu foil	-0.80	6.261	1.31×10^{-2}	
[G]	Li et al.[23]	OD-Cu foil	-0.85	5.702	1.19×10^{-2}	
[H]	Raciti et al.[24]	OD-Cu nanowires	-0.20	0.032	7.71×10^{-5}	Data from electrochemically reduced Cu nanowires. Total geometric current densities and Faradaic efficiencies were obtained from Figure 3. RF = 417, estimated from double layer capacitance obtained from CVs (Figure S6 and Table S3, Supporting Information).
[H]	Raciti et al.[24]	OD-Cu nanowires	-0.30	0.198	4.73×10^{-4}	
[H]	Raciti et al.[24]	OD-Cu nanowires	-0.40	0.498	1.19×10^{-3}	
[H]	Raciti et al.[24]	OD-Cu nanowires	-0.50	1.117	2.67×10^{-3}	
[H]	Raciti et al.[24]	OD-Cu nanowires	-0.60	6.091	1.45×10^{-2}	
[H]	Raciti et al.[24]	OD-Cu nanowires	-0.70	10.976	2.62×10^{-2}	
[H]	Raciti et al.[24]	OD-Cu nanowires	-0.80	14.739	3.52×10^{-2}	
[H]	Raciti et al.[24]	OD-Cu nanowires	-0.90	17.984	4.29×10^{-2}	
[H]	Raciti et al.[24]	OD-Cu nanowires	-1.00	20.862	4.98×10^{-2}	
[I]	Handoko et al.[25]	OD-Cu film	-0.68	0.942	0.010	Data from sample C, which represents an average film thickness of 3.7 μm.
[I]	Handoko et al.[25]	OD-Cu film	-0.78	2.880	0.030	
[I]	Handoko et al.[25]	OD-Cu film	-0.83	3.961	0.041	

[I]	Handoko et al.[25]	OD-Cu film	-0.88	5.062	0.053	Total geometric current densities were obtained from Figure S3k (Supporting Information). Faradaic efficiencies were obtained from Figure 3b. RF = 96, estimated from double layer capacitance obtained from CVs (Table 1), with a total geometric surface area of 0.38 cm^2 for the electrodes.
[I]	Handoko et al.[25]	OD-Cu film	-0.93	6.658	0.069	
[I]	Handoko et al.[25]	OD-Cu film	-0.98	11.822	0.123	
[I]	Handoko et al.[25]	OD-Cu film	-1.03	12.890	0.134	
[I]	Handoko et al.[25]	OD-Cu film	-1.08	10.783	0.112	
[I]	Handoko et al.[25]	OD-Cu film	-1.13	3.796	0.040	
[J]	Ren et al.[26]	OD-Cu film	-0.75	1.368	0.105	Data from NC-10 samples. Total geometric current densities and Faradaic efficiencies obtained from Table S6 (Supporting Information). RF = 13, estimated from double layer capacitance obtained from CVs (Table S2, Supporting Information).
[J]	Ren et al.[26]	OD-Cu film	-0.85	3.590	0.276	
[J]	Ren et al.[26]	OD-Cu film	-0.95	14.149	1.088	
[J]	Ren et al.[26]	OD-Cu film	-1.05	18.358	1.412	
[J]	Ren et al.[26]	OD-Cu film	-1.15	11.633	0.895	
[K]	Yang et al.[27]	Mesoporous Cu film	-0.70	--	0.030	Note: The authors only provided specific current density, and no geometric data. CO_2R specific current densities were obtained from Figure 3.
[K]	Yang et al.[27]	Mesoporous Cu film	-0.80	--	0.130	
[K]	Yang et al.[27]	Mesoporous Cu film	-0.90	--	0.240	
[K]	Yang et al.[27]	Mesoporous Cu film	-1.00	--	0.510	
[K]	Yang et al.[27]	Mesoporous Cu film	-1.10	--	0.870	
[K]	Yang et al.[27]	Mesoporous Cu film	-1.20	--	3.000	
[K]	Yang et al.[27]	Mesoporous Cu film	-1.30	--	6.000	
[K]	Yang et al.[27]	Mesoporous Cu film	-1.40	--	7.200	

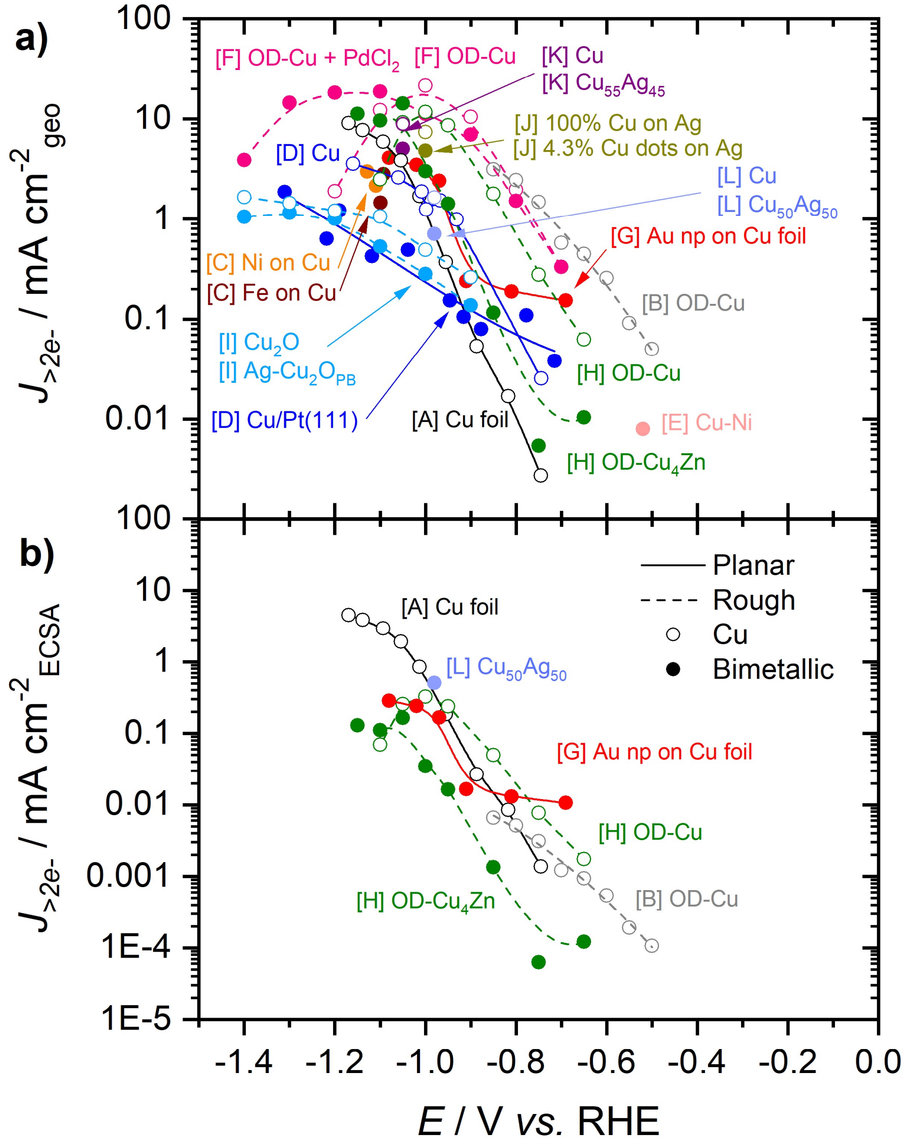

Figure 36: Cu-based bimetallic catalysts' total current density to further reduced (>2e$^-$) products normalized by **a)** the geometric area and **b)** the ECSA. The data were obtained from the following studies: [A] Cu foil by Kuhl *et al.*[16]; [B] OD-Cu by Li *et al.*[23]; [C] Ni and Fe deposits on Cu (two points shown for the beginning and end compositions formed by the *in-situ* electrodeposition) by Hori *et al.*[28]; [D] Cu overlayer on Pt(111) and Cu control sample by Varela *et al.*[29]; [E] $Cu_{90.5}Ni_{9.5}$ alloy by Watanabe *et al.*[30]; [F] OD-Cu with $PdCl_2$ in the electrolyte forming deposits on the surface, as well as an OD-Cu control sample, by Chen *et al.*[31]; [G] Au nanoparticles on Cu foil by Morales-Guio *et al.*[32]; [H] OD-Cu_4Zn and OC-Cu control sample by Ren *et al.*[33]; [I] Ag-Cu_2O_{PB} (PB = phase blended) and Cu_2O standard both deposited on Toray paper by Lee *et al.*[34]; [J] 4.3% Cu dots patterned on an Ag substrate and a 100% Cu (fully coated on Ag substrate) control sample by Lum *et al.*[35]; [K] $Cu_{55}Ag_{45}$ bimetallic foil and Cu foil standard by Clark *et al.*[36]; [L] $Cu_{50}Ag_{50}$ thin film bimetallic and Cu control sample by Higgins *et al.*[37]

Table S6: Tabulated Data for Figure 36, Cu-based bimetallic catalysts' total current density to further reduced (>$2e^-$) products

	1st Author *et al.*[ref]	**Catalyst**	**V *vs.* RHE**	**$J_{>2e^-}$ GEO (mA/cm^2)**	**$J_{>2e^-}$ ECSA (mA/cm^2)**	**Notes** *(Figure/Table references noted here refer to those within the article from which the data was obtained)*
[A]	Kuhl *et al.*[16]	Cu foil	-0.75	0.003	0.001	Geometric partial current densities (PCDs) for >$2e^-$ products obtained from Figure 6. Roughness factor (RF) ≈ 2 (from SI)
[A]	Kuhl *et al.*[16]	Cu foil	-0.82	0.017	0.009	
[A]	Kuhl *et al.*[16]	Cu foil	-0.89	0.054	0.027	
[A]	Kuhl *et al.*[16]	Cu foil	-0.96	0.371	0.186	
[A]	Kuhl *et al.*[16]	Cu foil	-1.01	1.703	0.851	
[A]	Kuhl *et al.*[16]	Cu foil	-1.05	3.841	1.920	
[A]	Kuhl *et al.*[16]	Cu foil	-1.09	5.888	2.944	
[A]	Kuhl *et al.*[16]	Cu foil	-1.14	7.709	3.855	
[A]	Kuhl *et al.*[16]	Cu foil	-1.17	9.047	4.523	
[B]	Li *et al.*[23]	OD-Cu	-0.50	0.050	1.061E-04	J_{tot} (geometric) and Faradaic efficiencies for >$2e^-$ products obtained from Table S1. OD-Cu data shown here is for the sample annealed at 500 °C for 12 hr, **RF = 475** (polycrystalline Cu capacitance = 29 μF → RF=1) (annealed at 500 °C for 12 hr sample capacitance = 13.9 mF → RF=475) *See Table S2 for more details*
[B]	Li *et al.*[23]	OD-Cu	-0.55	0.091	1.916E-04	
[B]	Li *et al.*[23]	OD-Cu	-0.60	0.257	5.406E-04	
[B]	Li *et al.*[23]	OD-Cu	-0.65	0.448	9.438E-04	
[B]	Li *et al.*[23]	OD-Cu	-0.70	0.578	1.217E-03	
[B]	Li *et al.*[23]	OD-Cu	-0.75	1.484	3.123E-03	
[B]	Li *et al.*[23]	OD-Cu	-0.80	2.448	5.153E-03	
[B]	Li *et al.*[23]	OD-Cu	-0.85	3.135	6.600E-03	
[C]	Hori *et al.*[28]	Ni on Cu	-1.11	2.150	N/A	Electroreduction at -5 mA/cm^2 on *in-situ* Ni- or Fe-modified Cu electrodes, Voltages and Faradaic efficiencies for >$2e^-$ products obtained from Figure 1. Coverage = 0.30 Ni (@ end, V_{RHE} = -1.11) Coverage = 0.04 Ni (@ start, V_{RHE} = -1.13) Coverage = 0.50 Fe (@ end, V_{RHE} = -1.10) Coverage = 0.08 Fe (@ start, V_{RHE} = -1.09) V_{SHE} obtained from Hori *et al.*, converted to V_{RHE} via: $V_{RHE} = V_{SHE} + 0.059pH = V_{SHE} + 0.059(6.8) = V_{SHE} + 0.40$ V
[C]	Hori *et al.*[28]	Ni on Cu	-1.13	2.985	N/A	
[C]	Hori *et al.*[28]	Fe on Cu	-1.10	1.450	N/A	
[C]	Hori *et al.*[28]	Fe on Cu	-1.09	2.815	N/A	
[D]	Varela *et al.*[29]	Cu on Pt(111)	-0.72	0.038	N/A	Voltages and CH_4 partial current densities obtained from Figure 4.
[D]	Varela *et al.*[29]	Cu on Pt(111)	-0.78	0.109	N/A	
[D]	Varela *et al.*[29]	Cu on Pt(111)	-0.88	0.080	N/A	

[D]	Varela *et al.*[29]	Cu on Pt(111)	-0.92	0.106	N/A	RF of single crystals assumed to be 1; however, due to the observed structural changes of the Cu overlayer during electrochemical testing, we did not feel comfortable maintaining this assumption. Thus, we used the given current density as the geometric current density.
[D]	Varela *et al.*[29]	Cu on Pt(111)	-0.95	0.153	N/A	
[D]	Varela *et al.*[29]	Cu on Pt(111)	-1.04	0.491	N/A	
[D]	Varela *et al.*[29]	Cu on Pt(111)	-1.12	0.426	N/A	
[D]	Varela *et al.*[29]	Cu on Pt(111)	-1.22	0.635	N/A	
[D]	Varela *et al.*[29]	Cu on Pt(111)	-1.19	1.220	N/A	
[D]	Varela *et al.*[29]	Cu on Pt(111)	-1.31	1.869	N/A	
[D]	Varela *et al.*[29]	Polycrystalline Cu control	-0.74	0.026	0.023	Voltages and CH_4 partial current densities obtained from Figure 4. Roughness factor of polycrystalline Cu foil determined via Pb UPD to be **RF=1.1**
[D]	Varela *et al.*[29]	Polycrystalline Cu control	-0.93	0.993	0.903	
[D]	Varela *et al.*[29]	Polycrystalline Cu control	-0.97	1.533	1.394	
[D]	Varela *et al.*[29]	Polycrystalline Cu control	-1.00	1.243	1.130	
[D]	Varela *et al.*[29]	Polycrystalline Cu control	-1.01	1.880	1.709	
[D]	Varela *et al.*[29]	Polycrystalline Cu control	-1.06	2.607	2.370	
[D]	Varela *et al.*[29]	Polycrystalline Cu control	-1.16	3.560	3.236	
[E]	Watanabe *et al.*[30]	$Cu_{90.5}Ni_{9.5}$ alloy	-0.52	0.008	N/A	Voltage obtained from Figure 1, and partial current density obtained from Table IV. V_{SHE} obtained from Watanabe *et al.*, converted to V_{RHE}: $V_{RHE} = V_{SHE} + 0.059pH = -0.9 + 0.059(6.4) = -0.52$ V
[F]	Chen *et al.*[31]	OD-Cu + $PdCl_2$	-0.7	0.33	N/A	Total current densities obtained from Figure 2B, and Faradaic efficiencies obtained from Table S3. RF is unclear due to the transient nature of the deposits formed from $PdCl_2$.
[F]	Chen *et al.*[31]	OD-Cu + $PdCl_2$	-0.8	1.52	N/A	
[F]	Chen *et al.*[31]	OD-Cu + $PdCl_2$	-0.9	6.96	N/A	
[F]	Chen *et al.*[31]	OD-Cu + $PdCl_2$	-1.0	11.21	N/A	
[F]	Chen *et al.*[31]	OD-Cu + $PdCl_2$	-1.1	18.74	N/A	
[F]	Chen *et al.*[31]	OD-Cu + $PdCl_2$	-1.2	18.19	N/A	
[F]	Chen *et al.*[31]	OD-Cu + $PdCl_2$	-1.3	14.50	N/A	
[F]	Chen *et al.*[31]	OD-Cu + $PdCl_2$	-1.4	3.90	N/A	
[F]	Chen *et al.*[31]	OD-Cu	-0.7	0.33	0.05	Total current densities obtained from Figure 2B, and Faradaic efficiencies obtained from Table S3.
[F]	Chen *et al.*[31]	OD-Cu	-0.8	1.95	0.30	

[F]	Chen *et al.*[31]	OD-Cu	-0.9	10.43	1.60	Authors state that this Cu_2O-derived Cu catalyst has a RF 6-7x larger than that of the electropolished Cu substrate; assuming that has RF=1, we can tentatively assume this RF≈6.5 (this ECSA-normalized data was not shown though)
[F]	Chen *et al.*[31]	OD-Cu	-1.0	21.43	3.30	
[F]	Chen *et al.*[31]	OD-Cu	-1.1	12.25	1.89	
[F]	Chen *et al.*[31]	OD-Cu	-1.2	1.89	0.29	
[G]	Morales-Guio *et al.*[32]	Au np on Cu foil	-0.69	0.153	0.011	V, PCD data obtained from Supplementary Table 3. Double layer capacitance (C_{dl}) data given in Supplementary Figure 3: (C_{dl} of Au/Cu as prepared = 692 μF cm^{-2}) (C_{dl} of Au/Cu after CO_2R = 418 μF cm^{-2}) (C_{dl} of Cu after CO_2R = 59 μF cm^{-2} → this sample is analogous to Kuhl *et al.* Cu foil, which has RF≈2) Thus, C_{dl} from Li *et al.* above (29 μF cm^{-2}) was used to obtain the roughness factor for Au np on Cu foil: **RF** = 418 μF cm^{-2}/29 μF cm^{-2} = **14.41**
[G]	Morales-Guio *et al.*[32]	Au np on Cu foil	-0.81	0.189	0.013	
[G]	Morales-Guio *et al.*[32]	Au np on Cu foil	-0.91	0.240	0.017	
[G]	Morales-Guio *et al.*[32]	Au np on Cu foil	-0.97	2.417	0.168	
[G]	Morales-Guio *et al.*[32]	Au np on Cu foil	-1.02	3.487	0.242	
[G]	Morales-Guio *et al.*[32]	Au np on Cu foil	-1.08	4.100	0.284	
[H]	Ren *et al.*[33]	OD-Cu_4Zn	-0.65	0.010	1.21E-04	Total current density data obtained from Figure 3, and average Faradaic efficiencies obtained from Table S8. Double layer capacitance (C_{dl}) data given in Table S3: OD-Cu_4Zn: 2500 μF cm^{-2} Cu metal ideally smooth surface: 29 μF cm^{-2} **RF OD-Cu_4Zn** = 2500 μF cm^{-2} / 29 μF cm^{-2} = **86.2**
[H]	Ren *et al.*[33]	OD-Cu_4Zn	-0.75	0.006	6.32E-05	
[H]	Ren *et al.*[33]	OD-Cu_4Zn	-0.85	0.116	1.40E-03	
[H]	Ren *et al.*[33]	OD-Cu_4Zn	-0.95	1.414	0.016	
[H]	Ren *et al.*[33]	OD-Cu_4Zn	-1.00	2.995	0.035	
[H]	Ren *et al.*[33]	OD-Cu_4Zn	-1.05	14.268	0.166	
[H]	Ren *et al.*[33]	OD-Cu_4Zn	-1.10	9.624	0.112	
[H]	Ren *et al.*[33]	OD-Cu_4Zn	-1.15	11.175	0.130	
[H]	Ren *et al.*[33]	OD-Cu	-0.65	0.063	0.002	Total current density data obtained from Figure 3, and average Faradaic efficiencies obtained from Table S5. Double layer capacitance (C_{dl}) data given in Table S3: OD-Cu: 1040 μF cm^{-2} Cu metal ideally smooth surface: 29 μF cm^{-2} **RF OD-Cu** = 1040 μF cm^{-2} / 29 μF cm^{-2} = **35.9**
[H]	Ren *et al.*[33]	OD-Cu	-0.75	0.277	0.008	
[H]	Ren *et al.*[33]	OD-Cu	-0.85	1.787	0.050	
[H]	Ren *et al.*[33]	OD-Cu	-0.95	8.564	0.239	
[H]	Ren *et al.*[33]	OD-Cu	-1.00	11.684	0.326	
[H]	Ren *et al.*[33]	OD-Cu	-1.05	9.192	0.256	
[H]	Ren *et al.*[33]	OD-Cu	-1.10	2.497	0.070	
[I]	Lee *et al.*[34]	Ag-Cu_2O_{PB}	-0.9	0.14	N/A	Total current density data obtained from Figure S6b, and Faradaic efficiency data obtained from Table S2. Ag-Cu_2O_{PB} → PB = phase blended
[I]	Lee *et al.*[34]	Ag-Cu_2O_{PB}	-1.0	0.28	N/A	
[I]	Lee *et al.*[34]	Ag-Cu_2O_{PB}	-1.1	0.53	N/A	
[I]	Lee *et al.*[34]	Ag-Cu_2O_{PB}	-1.2	1.00	N/A	
[I]	Lee *et al.*[34]	Ag-Cu_2O_{PB}	-1.3	1.15	N/A	

[I]	Lee *et al.*[34]	Ag-Cu_2O_{PB}	-1.4	1.05	N/A	
[I]	Lee *et al.*[34]	Cu_2O	-0.9	0.26	N/A	Total current density data obtained from Figure S6c, and Faradaic efficiency data obtained from Table S3.
[I]	Lee *et al.*[34]	Cu_2O	-1.0	0.49	N/A	
[I]	Lee *et al.*[34]	Cu_2O	-1.1	1.06	N/A	
[I]	Lee *et al.*[34]	Cu_2O	-1.2	1.20	N/A	
[I]	Lee *et al.*[34]	Cu_2O	-1.3	1.44	N/A	
[I]	Lee *et al.*[34]	Cu_2O	-1.4	1.65	N/A	
[J]	Lum *et al.*[35]	4.3% Cu dots on Ag	-1.0	4.82	N/A	Total current densities and Faradaic efficiency data for >2e$^-$ products obtained from Figure 7b.
[J]	Lum *et al.*[35]	100% Cu on Ag, control	-1.0	7.40	N/A	Total current densities and Faradaic efficiency data for >2e$^-$ products obtained from Figure 7b.
[K]	Clark *et al.*[36]	$Cu_{55}Ag_{45}$ foil	-1.05	5.03	N/A	Partial current densities for >2e$^-$ products obtained from Figure 3 (R-COOH, R-CHO, R-OH, and R-H).
[K]	Clark *et al.*[36]	Cu foil	-1.05	8.84	N/A	
[L]	Higgins *et al.*[37]	$Cu_{50}Ag_{50}$ thin film	-0.98	0.71	0.51	Partial current densities for >2e$^-$ products obtained from Table S4. RF = 1.104 determined by AFM.
[L]	Higgins *et al.*[37]	Cu thin film, control	-0.98	1.64	N/A	Partial current densities for >2e$^-$ products obtained from Table S4.

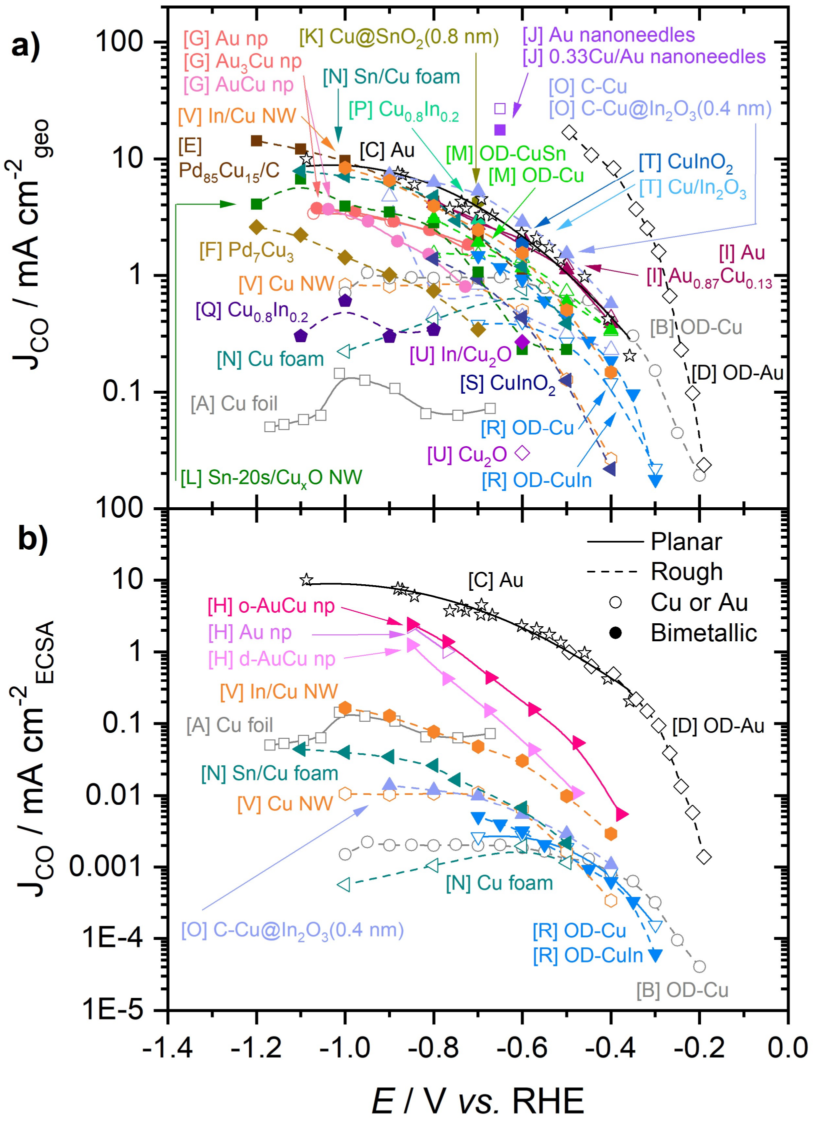

Figure 37: Cu-based bimetallic catalysts' total current density to CO production normalized by **a)** the geometric area and **b)** the ECSA. The data were obtained from the following studies: [A] Cu foil by Kuhl *et al.*[16]; [B] OD-Cu by Li *et al.*[23]; [C] Au by Hori *et al.*[38]; [D] OD-Au by Chen *et al.*[39]; [E] Pd$_{85}$Cu$_{15}$/C alloy nanoparticles supported on carbon black by Yin *et al.*[40]; [F] Pd$_7$Cu$_3$ electrodeposited mesoporous films by Li *et al.*[41]; [G] AuCu, Au$_3$Cu, and Au nanoparticles by Kim *et al.*[42]; [H] ordered (o-) and disordered (d-) AuCu nanoparticles and Au nanoparticle control sample by Kim *et al.*[43]; [I] Au and Au$_{0.87}$Cu$_{0.13}$ prepared by pulsed laser deposition in 220 mtorr O$_2$ by Roy *et al.*[44]; [J] 33% Cu coverage on Au nanoneedles and Au nanoneedles by Ross *et al.*[45]; [K] Cu@SnO$_2$(0.8 nm) core-shell nanoparticles by Li *et al.* [46]; [L] Sn deposited for 20 sec on Cu$_x$O nanowires by Zhao *et al.*[47]; [M] OD-CuSn and OD-Cu control sample by Sarfraz *et al.*[48]; [N] 2-3 at.% Sn on Cu10 foam (Sn/Cu foam) and Cu10 foam standard (Cu10 = 10 min electrodeposition) by Zeng *et al.*[49]; [O] Carbon-supported Cu@In$_2$O$_3$(0.4 nm) core-shell nanoparticles and carbon-supported Cu nanoparticle control sample by Xie *et al.*[50]; [P] Cu$_{0.8}$In$_{0.2}$ by He *et al.*[51]; [Q] Cu$_{0.8}$In$_{0.2}$ by Hoffman *et al.*[52]; [R] OD-CuIn and OD-Cu control sample by Rasul *et al.*[53]; [S] CuInO$_2$-derived by Jedidi *et al.*[54]; [T] Cu/In$_2$O$_3$-derived and CuInO$_2$-derived by Larrazábal *et al.*[55]; [U] In dots microfabricated on Cu$_2$O substrate (In/Cu$_2$O) and Cu$_2$O control sample by Larrazábal *et al.*[56]; [V] In deposited on Cu nanowires (Cu(OH)$_2$ derived) using 20 mM InCl$_3$ solution and Cu nanowire control sample by Luo *et al.*[57]

Table S7: Tabulated Data for Figure 37, Cu-based bimetallic catalysts' total current density to CO production

	1st Author *et al.*[ref]	**Catalyst**	**V *vs.* RHE**	**J_{CO} GEO (mA/cm^2)**	**J_{CO} ECSA (mA/cm^2)**	**Notes** *(Figure/Table references noted here refer to those within the article from which the data was obtained)*
[A]	Kuhl *et al.*[16]	Cu foil	-0.75 to -1.17			*Same as in Table S6 above*
[B]	Li *et al.*[23]	OD-Cu	-0.50 to -0.85			*Same as in Table S6 above*
[C]	Hori *et al.*[38]	Au	-0.36	0.204	0.204	CO Partial Current Densities (PCDs) obtained from Figure 1. Roughness factor (RF) was assumed to be ≈ 1 V_{SHE} obtained from Hori *et al.*, converted to V_{RHE} via: $V_{RHE} = V_{SHE} + 0.059pH = V_{SHE} + 0.059(7.5) = V_{SHE} + 0.44$ V
[C]	Hori *et al.*[38]	Au	-0.41	0.420	0.420	
[C]	Hori *et al.*[38]	Au	-0.46	0.974	0.974	
[C]	Hori *et al.*[38]	Au	-0.51	1.360	1.360	
[C]	Hori *et al.*[38]	Au	-0.54	1.754	1.754	
[C]	Hori *et al.*[38]	Au	-0.57	1.773	1.773	
[C]	Hori *et al.*[38]	Au	-0.57	2.100	2.100	
[C]	Hori *et al.*[38]	Au	-0.60	2.310	2.310	
[C]	Hori *et al.*[38]	Au	-0.67	3.261	3.261	
[C]	Hori *et al.*[38]	Au	-0.69	3.312	3.312	
[C]	Hori *et al.*[38]	Au	-0.69	4.508	4.508	
[C]	Hori *et al.*[38]	Au	-0.73	3.735	3.735	
[C]	Hori *et al.*[38]	Au	-0.74	4.273	4.273	
[C]	Hori *et al.*[38]	Au	-0.76	3.738	3.738	
[C]	Hori *et al.*[38]	Au	-0.84	5.978	5.978	
[C]	Hori *et al.*[38]	Au	-0.86	3.555	3.555	
[C]	Hori *et al.*[38]	Au	-0.87	7.335	7.335	
[C]	Hori *et al.*[38]	Au	-0.88	7.597	7.597	
[C]	Hori *et al.*[38]	Au	-1.09	9.988	9.988	
[D]	Chen *et al.*[39]	OD-Au	-0.19	0.024	0.001	CO PCDs and overpotentials obtained from Figure 4a; overpotentials converted to V_{RHE} based on $E^0(CO_2 \rightarrow CO) = -0.10$ V *vs.* RHE. ECSA determined by measuring anodic stripping waves for under-potential deposited Cu monolayers. A roughness factor (RF) of 72 was obtained after 15 min of electrolysis at −0.4 V, which is just long enough
[D]	Chen *et al.*[39]	OD-Au	-0.22	0.098	0.006	
[D]	Chen *et al.*[39]	OD-Au	-0.24	0.229	0.013	
[D]	Chen *et al.*[39]	OD-Au	-0.27	0.668	0.039	
[D]	Chen *et al.*[39]	OD-Au	-0.29	1.598	0.094	
[D]	Chen *et al.*[39]	OD-Au	-0.32	2.543	0.150	

[D]	Chen *et al.*[39]	OD-Au	-0.34	3.699	0.218	for complete reduction of the precursor Au oxide layer. After 8 hr, however, the RF was reduced to 17, indicating that sintering of Au NPs occurred during CO_2R electrolysis. Thus, **RF=17** was used.
[D]	Chen *et al.*[39]	OD-Au	-0.39	8.361	0.492	
[D]	Chen *et al.*[39]	OD-Au	-0.44	10.820	0.636	
[D]	Chen *et al.*[39]	OD-Au	-0.49	16.862	0.992	
[E]	Yin *et al.*[40]	$Pd_{85}Cu_{15}$/C	-0.6	1.01	N/A	V and CO PCD data obtained from Figure 3b.
[E]	Yin *et al.*[40]	$Pd_{85}Cu_{15}$/C	-0.7	2.18	N/A	
[E]	Yin *et al.*[40]	$Pd_{85}Cu_{15}$/C	-0.8	4.29	N/A	
[E]	Yin *et al.*[40]	$Pd_{85}Cu_{15}$/C	-0.9	6.92	N/A	
[E]	Yin *et al.*[40]	$Pd_{85}Cu_{15}$/C	-1.0	9.68	N/A	
[E]	Yin *et al.*[40]	$Pd_{85}Cu_{15}$/C	-1.1	12.12	N/A	
[E]	Yin *et al.*[40]	$Pd_{85}Cu_{15}$/C	-1.2	14.20	N/A	
[F]	Li *et al.*[41]	Pd_7Cu_3 mesoporous film	-0.7	0.34	N/A	J_{total} (geometric) and CO Faradaic efficiency data used to calculate PCDs were obtained from Figure 3a and Figure 3b, respectively.
[F]	Li *et al.*[41]	Pd_7Cu_3 mesoporous film	-0.8	0.74	N/A	
[F]	Li *et al.*[41]	Pd_7Cu_3 mesoporous film	-0.9	1.02	N/A	
[F]	Li *et al.*[41]	Pd_7Cu_3 mesoporous film	-1.0	1.43	N/A	
[F]	Li *et al.*[41]	Pd_7Cu_3 mesoporous film	-1.1	2.22	N/A	
[F]	Li *et al.*[41]	Pd_7Cu_3 mesoporous film	-1.2	2.58	N/A	
[G]	Kim *et al.*[42]	Au_3Cu nps	-0.7	1.84	N/A	J_{total} (geometric) and CO Faradaic efficiency data used to calculate PCDs were obtained from Figure 2a and Figure 2c, respectively.
[G]	Kim *et al.*[42]	Au_3Cu nps	-0.8	2.45	N/A	
[G]	Kim *et al.*[42]	Au_3Cu nps	-0.9	2.91	N/A	
[G]	Kim *et al.*[42]	Au_3Cu nps	-1.0	3.52	N/A	
[G]	Kim *et al.*[42]	Au_3Cu nps	-1.1	3.75	N/A	
[G]	Kim *et al.*[42]	AuCu nps	-0.7	0.80	N/A	J_{total} (geometric) and CO Faradaic efficiency data used to calculate PCDs were obtained from Figure 2a and Figure 2d, respectively.
[G]	Kim *et al.*[42]	AuCu nps	-0.8	1.52	N/A	
[G]	Kim *et al.*[42]	AuCu nps	-0.9	1.95	N/A	
[G]	Kim *et al.*[42]	AuCu nps	-1.0	2.91	N/A	
[G]	Kim *et al.*[42]	AuCu nps	-1.1	3.69	N/A	
[G]	Kim *et al.*[42]	Au nps	-0.7	1.64	N/A	
[G]	Kim *et al.*[42]	Au nps	-0.8	2.45	N/A	

[G]	Kim *et al.*[42]	Au nps	-0.9	2.91	N/A	J_{total} (geometric) and CO Faradaic efficiency data used to calculate PCDs were obtained from Figure 2a and Figure 2b, respectively.
[G]	Kim *et al.*[42]	Au nps	-0.9	3.39	N/A	
[G]	Kim *et al.*[42]	Au nps	-1.0	3.39	N/A	
[H]	Kim *et al.*[43]	o-AuCu nps	-0.38	N/A	0.005	V and J_{CO} (ECSA normalized) data obtained from Figure S18. CO PCDs are specific current densities based on actual surface area of nanoparticle (np) catalysts measured by Cu underpotential deposition on o-AuCu and Au nps.
[H]	Kim *et al.*[43]	o-AuCu nps	-0.48	N/A	0.054	
[H]	Kim *et al.*[43]	o-AuCu nps	-0.58	N/A	0.158	
[H]	Kim *et al.*[43]	o-AuCu nps	-0.67	N/A	0.440	
[H]	Kim *et al.*[43]	o-AuCu nps	-0.77	N/A	1.391	
[H]	Kim *et al.*[43]	o-AuCu nps	-0.85	N/A	2.424	
[H]	Kim *et al.*[43]	d-AuCu nps	-0.48	N/A	0.011	V and J_{CO} (ECSA normalized) data obtained from Figure S18. CO PCDs are specific current densities based on actual surface area of nanoparticle (np) catalysts measured by Cu underpotential deposition on o-AuCu and Au nps.
[H]	Kim *et al.*[43]	d-AuCu nps	-0.58	N/A	0.043	
[H]	Kim *et al.*[43]	d-AuCu nps	-0.68	N/A	0.152	
[H]	Kim *et al.*[43]	d-AuCu nps	-0.77	N/A	0.424	
[H]	Kim *et al.*[43]	d-AuCu nps	-0.85	N/A	1.250	
[H]	Kim *et al.*[43]	Au nps	-0.77	N/A	1.022	V and J_{CO} (ECSA normalized) data obtained from Figure 4 (-0.77 V) and Figure S19 (-0.85 V).
[H]	Kim *et al.*[43]	Au nps	-0.85	N/A	2.264	
[I]	Roy *et al.*[44]	$Au_{0.87}Cu_{0.13}$	-0.4	0.38	N/A	V and J_{CO} (geometric) data obtained from Figure 7f. Film made by pulsed laser deposition in 220 mtorr O_2.
[I]	Roy *et al.*[44]	$Au_{0.87}Cu_{0.13}$	-0.5	1.12	N/A	
[I]	Roy *et al.*[44]	$Au_{0.87}Cu_{0.13}$	-0.6	2.16	N/A	
[I]	Roy *et al.*[44]	$Au_{0.87}Cu_{0.13}$	-0.7	2.68	N/A	
[I]	Roy *et al.*[44]	$Au_{0.87}Cu_{0.13}$	-0.8	4.48	N/A	
[I]	Roy *et al.*[44]	Au	-0.4	0.43	N/A	V and J_{CO} (geometric) data obtained from Figure 7f. Film made by pulsed laser deposition in 220 mtorr O_2.
[I]	Roy *et al.*[44]	Au	-0.5	1.21	N/A	
[I]	Roy *et al.*[44]	Au	-0.6	1.77	N/A	
[I]	Roy *et al.*[44]	Au	-0.7	3.07	N/A	
[I]	Roy *et al.*[44]	Au	-0.8	4.14	N/A	
[J]	Ross *et al.*[45]	33% monolayer of Cu on Au nanoneedles	-0.65	17.6	N/A	V and J_{CO} (geometric) data obtained from Figure 4c.
[J]	Ross *et al.*[45]	Au nanoneedles	-0.65	26.8	N/A	V and J_{CO} (geometric) data obtained from Figure 4c.
[K]	Li *et al.* [46]	Cu@SnO_2 (0.8 nm) nps	-0.7	4.278	N/A	CO PCD obtained from "highest FE achieves 93% at −0.7 V with the current density of 4.6 mA/cm^2"
[L]	Zhao *et al.*[47]	Sn-20s/Cu_xO NW	-0.5	0.23	N/A	V and J_{CO} (geometric) data for Sn-20s/Cu_xO NWs (Sn deposited for 20 sec on Cu_xO NWs) obtained from Figure 4a.
[L]	Zhao *et al.*[47]	Sn-20s/Cu_xO NW	-0.6	0.23	N/A	
[L]	Zhao *et al.*[47]	Sn-20s/Cu_xO NW	-0.7	1.06	N/A	

[L]	Zhao *et al.*[47]	Sn-20s/Cu_xO NW	-0.8	2.82	N/A	
[L]	Zhao *et al.*[47]	Sn-20s/Cu_xO NW	-0.9	3.49	N/A	
[L]	Zhao *et al.*[47]	Sn-20s/Cu_xO NW	-1.0	3.90	N/A	
[L]	Zhao *et al.*[47]	Sn-20s/Cu_xO NW	-1.1	6.68	N/A	
[L]	Zhao *et al.*[47]	Sn-20s/Cu_xO NW	-1.2	4.06	N/A	
[M]	Sarfraz *et al.*[48]	OD-CuSn	-0.4	0.34	N/A	J_{total} (geometric) and CO Faradaic efficiency data used to calculate PCDs were obtained from Figure 2 and Figure 3b, respectively.
[M]	Sarfraz *et al.*[48]	OD-CuSn	-0.5	0.59	N/A	
[M]	Sarfraz *et al.*[48]	OD-CuSn	-0.6	1.16	N/A	
[M]	Sarfraz *et al.*[48]	OD-CuSn	-0.7	1.92	N/A	
[M]	Sarfraz *et al.*[48]	OD-CuSn	-0.8	3.07	N/A	
[M]	Sarfraz *et al.*[48]	OD-Cu control	-0.4	0.33	N/A	J_{total} (geometric) and CO Faradaic efficiency data used to calculate PCDs were obtained from Figure 2 and Figure 3a, respectively.
[M]	Sarfraz *et al.*[48]	OD-Cu control	-0.5	0.73	N/A	
[M]	Sarfraz *et al.*[48]	OD-Cu control	-0.6	1.40	N/A	
[M]	Sarfraz *et al.*[48]	OD-Cu control	-0.7	1.51	N/A	
[M]	Sarfraz *et al.*[48]	OD-Cu control	-0.8	1.55	N/A	
[N]	Zeng *et al.*[49]	Sn/Cu foam	-0.50	0.4	2.16E-03	Sn/Cu foam = 2-3 at.% Sn on Cu10 foam and Cu10 foam standard (Cu10 = 10 min electrodeposition). V and J_{CO} (geometric) data obtained from Figure 7. Double layer capacitance (C_{dl}) data obtained from CVs as shown in Figure S2: Cu foil = 0.028 mF cm^{-2} → (RF = 1) Cu10 foam = 12.6 mF cm^{-2} → (RF = 450) [Sn/Cu foam not measured with this technique] C_{dls} were also calculated via EIS data (see pg. 479): Cu10 foam = 11 mF cm^{-2} → (**RF = 392.9**) Sn/Cu foam = 5 mF cm^{-2} → (**RF = 178.6**) *To use the same method, the RFs used for Sn/Cu foam and Cu foam were those determined from EIS data.*
[N]	Zeng *et al.*[49]	Sn/Cu foam	-0.60	1.2	6.72E-03	
[N]	Zeng *et al.*[49]	Sn/Cu foam	-0.75	3.0	1.66E-02	
[N]	Zeng *et al.*[49]	Sn/Cu foam	-0.80	4.7	2.63E-02	
[N]	Zeng *et al.*[49]	Sn/Cu foam	-0.90	6.2	3.47E-02	
[N]	Zeng *et al.*[49]	Sn/Cu foam	-1.00	7.2	4.01E-02	
[N]	Zeng *et al.*[49]	Sn/Cu foam	-1.10	7.9	4.42E-02	
[N]	Zeng *et al.*[49]	Cu foam	-0.50	0.5	1.15E-03	
[N]	Zeng *et al.*[49]	Cu foam	-0.60	0.8	1.95E-03	
[N]	Zeng *et al.*[49]	Cu foam	-0.80	0.4	1.05E-03	
[N]	Zeng *et al.*[49]	Cu foam	-1.00	0.2	5.67E-04	
[O]	Xie *et al.*[50]	C-Cu@In_2O_3(0.4 nm) nps	-0.4	0.57	1.08E-03	Total current density data and CO Faradaic efficiencies used to calculate PCDs were obtained from Figure 6a and Figure 5b, respectively. It is given on pg. 37001 that the ECSA (as determined through calculating the double-layer charging currents)
[O]	Xie *et al.*[50]	C-Cu@In_2O_3(0.4 nm) nps	-0.5	1.53	2.91E-03	
[O]	Xie *et al.*[50]	C-Cu@In_2O_3(0.4 nm) nps	-0.6	2.86	5.44E-03	

[O]	Xie *et al.*[50]	C-Cu@In$_2$O$_3$(0.4 nm) nps	-0.7	5.27	1.00E-02	of C-Cu@In$_2$O$_3$(0.4 nm) is 35.1 m^2/g, and the 1 cm^2 electrode is coated on both sides by a total of 3 mg of catalyst. Thus, the RF was calculated: $RF = 35.1\ \frac{m^2}{g} \times \frac{0.003\ g\ catalyst}{2\ cm^2\ electrode\ area} \times \frac{10^4\ cm^2}{m^2}$ **RF = 526.5**
[O]	Xie *et al.*[50]	C-Cu@In$_2$O$_3$(0.4 nm) nps	-0.8	6.27	1.19E-02	
[O]	Xie *et al.*[50]	C-Cu@In$_2$O$_3$(0.4 nm) nps	-0.9	7.33	1.39E-02	
[O]	Xie *et al.*[50]	C-Cu nps	-0.4	0.23	N/A	Total current density data and CO Faradaic efficiencies used to calculate PCDs were obtained from Figure 6a and Figure 5a, respectively. The ECSA for C-Cu nps control sample was not provided.
[O]	Xie *et al.*[50]	C-Cu nps	-0.5	0.32	N/A	
[O]	Xie *et al.*[50]	C-Cu nps	-0.6	0.44	N/A	
[O]	Xie *et al.*[50]	C-Cu nps	-0.7	0.83	N/A	
[O]	Xie *et al.*[50]	C-Cu nps	-0.8	0.45	N/A	
[O]	Xie *et al.*[50]	C-Cu nps	-0.9	4.73	N/A	
[P]	He *et al.*[51]	Cu$_{0.8}$In$_{0.2}$	-0.7	3	N/A	Given on pg. 6071 that the "maximum CD·FE (PCD) for CO formation is approximately 3 mA cm^{-2} for films produced from alloys with stoichiometries of Cu$_{0.8}$In$_{0.2}$"
[Q]	Hoffman *et al.*[52]	Cu$_{0.8}$In$_{0.2}$	-0.8	0.34	N/A	V and J$_{CO}$ (geometric) data obtained from Figure 11c.
[Q]	Hoffman *et al.*[52]	Cu$_{0.8}$In$_{0.2}$	-0.9	0.30	N/A	
[Q]	Hoffman *et al.*[52]	Cu$_{0.8}$In$_{0.2}$	-1.0	0.60	N/A	
[Q]	Hoffman *et al.*[52]	Cu$_{0.8}$In$_{0.2}$	-1.1	0.30	N/A	
[R]	Rasul *et al.*[53]	OD-CuIn	-0.30	0.018	6.055E-05	J$_{total}$ (geometric) and CO Faradaic efficiencies used to calculate PCDs were obtained from Figure 1. Table S1 gives the capacitance values determined via CVs at different scan rates: Cu-sheet = 29 µF → RF = 1 ODCuIn = 8.5 mF → **RF = 293** OD-Cu = 4.2 mF → **RF = 143**
[R]	Rasul *et al.*[53]	OD-CuIn	-0.35	0.097	3.303E-04	
[R]	Rasul *et al.*[53]	OD-CuIn	-0.40	0.185	6.308E-04	
[R]	Rasul *et al.*[53]	OD-CuIn	-0.45	0.272	9.293E-04	
[R]	Rasul *et al.*[53]	OD-CuIn	-0.50	0.430	1.468E-03	
[R]	Rasul *et al.*[53]	OD-CuIn	-0.55	0.603	2.059E-03	
[R]	Rasul *et al.*[53]	OD-CuIn	-0.60	0.928	3.167E-03	
[R]	Rasul *et al.*[53]	OD-CuIn	-0.65	1.165	3.977E-03	
[R]	Rasul *et al.*[53]	OD-CuIn	-0.70	1.472	5.022E-03	
[R]	Rasul *et al.*[53]	OD-Cu control	-0.30	0.022	1.547E-04	
[R]	Rasul *et al.*[53]	OD-Cu control	-0.40	0.120	8.405E-04	
[R]	Rasul *et al.*[53]	OD-Cu control	-0.50	0.266	1.861E-03	
[R]	Rasul *et al.*[53]	OD-Cu control	-0.60	0.398	2.784E-03	
[R]	Rasul *et al.*[53]	OD-Cu control	-0.70	0.376	2.631E-03	
[S]	Jedidi *et al.*[54]	CuInO$_2$-derived	-0.4	0.022	N/A	J$_{total}$ (geometric) and CO Faradaic efficiencies used to calculate PCDs were obtained from Figure 3.
[S]	Jedidi *et al.*[54]	CuInO$_2$-derived	-0.5	0.126	N/A	

[S]	Jedidi *et al.*[54]	CuInO$_2$-derived	-0.6	0.433	N/A	
[S]	Jedidi *et al.*[54]	CuInO$_2$-derived	-0.7	0.935	N/A	
[S]	Jedidi *et al.*[54]	CuInO$_2$-derived	-0.8	1.387	N/A	
[T]	Larrazábal *et al.*[55]	Cu/In$_2$O$_3$-derived	-0.6	1.5	N/A	V and J_{CO} (geometric) data obtained from Figure 3a.
[T]	Larrazábal *et al.*[55]	CuInO$_2$-derived	-0.6	1.9	N/A	V and J_{CO} (geometric) data obtained from Figure 3a.
[U]	Larrazábal *et al.*[56]	In dots/Cu$_2$O	-0.6	0.268	N/A	J_{CO} (geometric) data for In/Cu$_2$O sample with d = 1.25 μm obtained from Figure 3.
[U]	Larrazábal *et al.*[56]	Cu$_2$O control	-0.6	0.030	N/A	J_{CO} (geometric) data for Cu$_2$O sample obtained from inset of Figure 2a.
[V]	Luo *et al.*[57]	In/Cu NW	-0.4	0.15	2.90E-03	Best sample was that deposited using 20 mM InCl$_3$ bath (CuIn20 NWs). V and J_{CO} (geometric) data obtained from Figure 3d. C_{dl} data obtained from Table S1: Electropolished Cu foil = 0.0474 mF cm^{-2} → RF = 1 CuIn20 NW = 3.7 mF cm^{-2} → **RF = 78**
[V]	Luo *et al.*[57]	In/Cu NW	-0.5	0.50	9.87E-03	
[V]	Luo *et al.*[57]	In/Cu NW	-0.6	1.56	3.05E-02	
[V]	Luo *et al.*[57]	In/Cu NW	-0.7	2.45	4.81E-02	
[V]	Luo *et al.*[57]	In/Cu NW	-0.8	3.93	7.71E-02	
[V]	Luo *et al.*[57]	In/Cu NW	-0.9	6.51	1.28E-01	
[V]	Luo *et al.*[57]	In/Cu NW	-1.0	8.40	1.65E-01	
[V]	Luo *et al.*[57]	Cu NW control	-0.4	0.03	3.42E-04	V and J_{CO} (geometric) data obtained from Figure 3d. C_{dl} data obtained from Table S1: Electropolished Cu foil = 0.0474 mF cm^{-2} → RF = 1 Cu NW control = 2.4 mF cm^{-2} → **RF = 51**
[V]	Luo *et al.*[57]	Cu NW control	-0.5	0.13	1.64E-03	
[V]	Luo *et al.*[57]	Cu NW control	-0.6	0.50	6.41E-03	
[V]	Luo *et al.*[57]	Cu NW control	-0.7	0.86	1.10E-02	
[V]	Luo *et al.*[57]	Cu NW control	-0.8	0.84	1.07E-02	
[V]	Luo *et al.*[57]	Cu NW control	-0.9	0.81	1.04E-02	
[V]	Luo *et al.*[57]	Cu NW control	-1.0	0.83	1.06E-02	

References

(1) Hori, Y.; Takahashi, R.; Yoshinami, Y.; Murata, A. Electrochemical Reduction of CO at a Copper Electrode. *J. Phys. Chem. B* **1997**, *101*, 7075–7081.

(2) Jouny, M.; Luc, W.; Jiao, F. General Techno-Economic Analysis of CO2 Electrolysis Systems. *Ind. Eng. Chem. Res.* **2018**, *57*, 2165–2177.

(3) Nie, X.; Esopi, M. R.; Janik, M. J.; Asthagiri, A. Selectivity of CO2 Reduction on Copper Electrodes: The Role of the Kinetics of Elementary Steps. *Angew. Chemie Int. Ed.* **2013**, *52*, 2459–2462.

(4) Nie, X.; Luo, W.; Janik, M. J.; Asthagiri, A. Reaction Mechanisms of CO2 Electrochemical Reduction on Cu(111) Determined with Density Functional Theory. *J. Catal.* **2014**, *312*, 108–122.

(5) Luo, W.; Nie, X.; Janik, M. J.; Asthagiri, A. Facet Dependence of CO2 Reduction Paths on Cu Electrodes. *ACS Catal.* **2016**, *6*, 219–229.

(6) Cheng, T.; Xiao, H.; Goddard, W. A. Reaction Mechanisms for the Electrochemical Reduction of CO2 to CO and Formate on the Cu(100) Surface at 298 K from Quantum Mechanics Free Energy Calculations with Explicit Water. *J. Am. Chem. Soc.* **2016**, *138*, 13802–13805.

(7) Liu, X.; Xiao, J.; Peng, H.; Hong, X.; Chan, K.; Nørskov, J. K. Understanding Trends in Electrochemical Carbon Dioxide Reduction Rates. *Nat. Commun.* **2017**, *8*, 15438.

(8) Ou, L.; Long, W.; Chen, Y.; Jin, J.-L. A New Reduction Mechanism of CO Dimer by Hydrogenation into C2H4 on Cu(100) Surface: A Theoretical Insight into Kinetics of Elementary Steps. *RSC Adv.* **2015**, 10.1039/C5RA15905A.

(9) Goodpaster, J. D.; Bell, A. T.; Head-Gordon, M. Identification of Possible Pathways for C-C Bond Formation during Electrochemical Reduction of CO2: New Theoretical Insights from an Improved Electrochemical Model. *J. Phys. Chem. Lett.* **2016**, *7*, 1471–1477.

(10) Xiao, H.; Cheng, T.; Goddard, W. A.; Sundararaman, R. Mechanistic Explanation of the PH Dependence and Onset Potentials for Hydrocarbon Products from Electrochemical Reduction of CO on Cu (111). *J. Am. Chem. Soc.* **2016**, *138*, 483–486.

(11) Cheng, T.; Xiao, H.; Goddard, W. A. Free-Energy Barriers and Reaction Mechanisms for the Electrochemical Reduction of CO on the Cu(100) Surface, Including Multiple Layers of Explicit Solvent at PH 0. *J. Phys. Chem. Lett.* **2015**, *6*, 4767–4773.

(12) Cheng, T.; Xiao, H.; Goddard, W. A. Full Atomistic Reaction Mechanism with Kinetics for CO Reduction on Cu(100) from Ab Initio Molecular Dynamics Free-Energy Calculations at 298 K. *Proc. Natl. Acad. Sci.* **2017**, *114*, 1795–1800.

(13) Calle-Vallejo, F.; Koper, M. T. M. Theoretical Considerations on the Electroreduction of CO to C2 Species on Cu(100) Electrodes. *Angew. Chemie - Int. Ed.* **2013**, *52*, 7282–7285.

(14) Garza, A.; Bell, A. T.; Head-Gordon, M. On the Mechanism of CO2 Reduction at Copper Surfaces: Pathways to C2 Products. *ACS Catal.* **2018**, *8*, 1490–1499.

(15) Sandberg, R. B.; Montoya, J. H.; Chan, K.; N??rskov, J. K.; Nørskov, J. K. CO-CO Coupling on Cu Facets: Coverage, Strain and Field Effects. *Surf. Sci.* **2016**, *654*, 56–62.

(16) Kuhl, K. P.; Cave, E. R.; Abram, D. N.; Jaramillo, T. F. New Insights into the Electrochemical Reduction of Carbon Dioxide on Metallic Copper Surfaces. *Energy Environ. Sci.* **2012**, *5*, 7050–7059.

(17) Hori, Y.; Wakebe, H.; Tsukamoto, T.; Koga, O. Electrocatalytic Process of CO Selectivity in Electrochemical Reduction of CO2 at Metal Electrodes in Aqueous Media. *Electrochim. Acta* **1994**, *39*, 1833–1839.

(18) Kwon, Y.; Lum, Y.; Clark, E. L.; Ager, J. W.; Bell, A. T. CO2 Electroreduction with Enhanced Ethylene and Ethanol Selectivity by Nanostructuring Polycrystalline Copper. *ChemElectroChem* **2016**, *3*, 1012–1019.

(19) Mistry, H.; Varela, A. S.; Bonifacio, C. S.; Zegkinoglou, I.; Sinev, I.; Choi, Y.; Kisslinger, K.; Stach, E. A.; Yang, J. C.; Strasser, P.; et al. Highly Selective Plasma-Activated Copper Catalysts for Carbon Dioxide Reduction to Ethylene. *Nat. Commun.* **2016**, *7*, 1–8.

(20) Min, S.; Yang, X.; Lu, A. Y.; Tseng, C. C.; Hedhili, M. N.; Li, L. J.; Huang, K. W. Low Overpotential and High Current CO2 Reduction with Surface Reconstructed Cu Foam Electrodes. *Nano Energy* **2016**, *27*, 121–129.

(21) Ma, M.; Djanashvili, K.; Smith, W. A. Selective Electrochemical Reduction of CO2 to CO on CuO-Derived Cu Nanowires. *Phys. Chem. Chem. Phys.* **2015**, *17*, 20861–20867.

(22) Ma, M.; Djanashvili, K.; Smith, W. A. Controllable Hydrocarbon Formation from the Electrochemical Reduction of CO2 over Cu Nanowire Arrays. *Angew. Chemie Int. Ed.* **2016**, *55*, 6680–6684.

(23) Li, C. W.; Kanan, M. W. CO2 Reduction at Low Overpotential on Cu Electrodes Resulting from the Reduction of Thick Cu2O Films. *J. Am. Chem. Soc.* **2012**, *134*, 7231–7234.

(24) Raciti, D.; Livi, K. J.; Wang, C. Highly Dense Cu Nanowires for Low-Overpotential CO2 Reduction. *Nano Lett.* **2015**, *15*, 6829–6835.

(25) Handoko, A. D.; Ong, C. W.; Huang, Y.; Lee, Z. G.; Lin, L.; Panetti, G. B.; Yeo, B. S. Mechanistic Insights into the Selective Electroreduction of Carbon Dioxide to Ethylene on Cu2O-Derived Copper Catalysts. *J. Phys. Chem. C* **2016**, *120*, 20058–20067.

(26) Ren, D.; Wong, N. T.; Handoko, A. D.; Huang, Y.; Yeo, B. S. Mechanistic Insights into the Enhanced Activity and Stability of Agglomerated Cu Nanocrystals for the Electrochemical Reduction of Carbon Dioxide to N-Propanol. *J. Phys. Chem. Lett.* **2016**, *7*, 20–24.

(27) Yang, K. D.; Ko, W. R.; Lee, J. H.; Kim, S. J.; Lee, H.; Lee, M. H.; Nam, K. T. Morphology-Directed Selective Production of Ethylene or Ethane from CO2 on a Cu Mesopore Electrode. *Angew. Chemie Int. Ed.* **2016**, *56*, 796–800.

(28) Hori, Y.; Murata, A.; Ito, S.; Yoshinami, Y.; Koga, O. Nickel and Iron Modified Copper Electrode for Electroreduction of CO2 by In-Situ Electrodeposition. *Chem. Lett.* **1989**, *18*, 1567–1570.

(29) Varela, A. S.; Schlaup, C.; Jovanov, Z. P.; Malacrida, P.; Horch, S.; Stephens, I. E. L.; Chorkendorff, I. CO2 Electroreduction on Well-Defined Bimetallic Surfaces: Cu Overlayers on Pt(111) and Pt(211). *J. Phys. Chem. C* **2013**, *117*, 20500–20508.

(30) Watanabe, M. Design of Alloy Electrocatalysts for CO2 Reduction: III. The Selective and Reversible Reduction of CO2 on Cu Alloy Electrodes. *J. Electrochem. Soc.* **1991**, *138*, 3382–3389.

(31) Chen, C. S.; Wan, J. H.; Yeo, B. S. Electrochemical Reduction of Carbon Dioxide to Ethane Using Nanostructured Cu2O-Derived Copper Catalyst and

Palladium(II) Chloride. *J. Phys. Chem. C* **2015**, *119*, 26875–26882.

(32) Morales-Guio, C. G.; Cave, E. R.; Nitopi, S. A.; Feaster, J. T.; Wang, L.; Kuhl, K. P.; Jackson, A.; Johnson, N. C.; Abram, D. N.; Hatsukade, T.; et al. Improved CO2 Reduction Activity towards C2+ Alcohols on a Tandem Au on Cu Electrocatalyst. *Nat. Catal.* **2018**, *1*, 764–771.

(33) Ren, D.; Ang, B. S.-H.; Yeo, B. S. Tuning the Selectivity of Carbon Dioxide Electroreduction toward Ethanol on Oxide-Derived CuxZn Catalysts. *ACS Catal.* **2016**, *6*, 8239–8247.

(34) Lee, S.; Park, G.; Lee, J. Importance of Ag-Cu Biphasic Boundaries for Selective Electrochemical Reduction of CO2 to Ethanol. *ACS Catal.* **2017**, *7*, 8594–8604.

(35) Lum, Y.; Ager, J. W. Sequential Catalysis Controls Selectivity in Electrochemical CO2 Reduction on Cu. *Energy Environ. Sci.* **2018**, *11*, 2935–2944.

(36) Clark, E. L.; Hahn, C.; Jaramillo, T. F.; Bell, A. T. Electrochemical CO2 Reduction over Compressively Strained CuAg Surface Alloys with Enhanced Multi-Carbon Oxygenate Selectivity. *J. Am. Chem. Soc.* **2017**, *139*, 15848–15857.

(37) Higgins, D.; Landers, A. T.; Ji, Y.; Nitopi, S.; Morales-Guio, C. G.; Wang, L.; Chan, K.; Hahn, C.; Jaramillo, T. F. Guiding Electrochemical Carbon Dioxide Reduction toward Carbonyls Using Copper Silver Thin Films with Interphase Miscibility. *ACS Energy Lett.* **2018**, *3*, 2947–2955.

(38) Hori, Y.; Murata, A.; Kikuchi, K.; Suzuki, S. Electrochemical Reduction of Carbon Dioxides to Carbon Monoxide at a Gold Electrode in Aqueous Potassium Hydrogen Carbonate. *J. Chem. Soc. Chem. Commun.* **1987**, *0*, 728.

(39) Chen, Y.; Li, C. W.; Kanan, M. W. Aqueous CO2 Reduction at Very Low Overpotential on Oxide-Derived Au Nanoparticles. *J. Am. Chem. Soc.* **2012**, *134*, 19969–19972.

(40) Yin, Z.; Gao, D.; Yao, S.; Zhao, B.; Cai, F.; Lin, L.; Tang, P.; Zhai, P.; Wang, G.; Ma, D.; et al. Highly Selective Palladium-Copper Bimetallic Electrocatalysts for the Electrochemical Reduction of CO2 to CO. *Nano Energy* **2016**, *27*, 35–43.

(41) Li, M.; Wang, J. J.; Li, P.; Chang, K.; Li, C. L.; Wang, T.; Jiang, B.; Zhang, H. B.; Liu, H. M.; Yamauchi, Y.; et al. Mesoporous Palladium-Copper Bimetallic Electrodes for Selective Electrocatalytic Reduction of Aqueous CO2 to CO. *J. Mater. Chem. A* **2016**, *4*, 4776–4782.

(42) Kim, D.; Resasco, J.; Yu, Y.; Asiri, A. M.; Yang, P. Synergistic Geometric and Electronic Effects for Electrochemical Reduction of Carbon Dioxide Using Gold-Copper Bimetallic Nanoparticles. *Nat. Commun.* **2014**, *5*, 4948.

(43) Kim, D.; Xie, C.; Becknell, N.; Yu, Y.; Karamad, M.; Chan, K.; Crumlin, E. J.; Nørskov, J. K.; Yang, P. Electrochemical Activation of CO2 through Atomic Ordering Transformations of AuCu Nanoparticles. *J. Am. Chem. Soc.* **2017**, *139*, 8329–8336.

(44) Roy, C.; Galipaud, J.; Fréchette-Viens, L.; Garbarino, S.; Qiao, J.; Guay, D. CO2 Electroreduction at AuxCu1-x Obtained by Pulsed Laser Deposition in O2 Atmosphere. *Electrochim. Acta* **2017**, *246*, 115–122.

(45) Ross, M. B.; Dinh, C. T.; Li, Y.; Kim, D.; De Luna, P.; Sargent, E. H.; Yang, P. Tunable Cu Enrichment Enables Designer Syngas Electrosynthesis from CO2. *J. Am. Chem. Soc.* **2017**, *139*, 9359–9363.

(46) Li, Q.; Fu, J.; Zhu, W.; Chen, Z.; Shen, B.; Wu, L.; Xi, Z.; Wang, T.; Lu, G.; Zhu, J.; et al. Tuning Sn-Catalysis for Electrochemical Reduction of CO2 to CO via the Core/Shell Cu/SnO2 Structure. *J. Am. Chem. Soc.* **2017**, *139*, 4290–4293.

(47) Zhao, Y.; Wang, C.; Wallace, G. G. Tin Nanoparticles Decorated Copper Oxide Nanowires for Selective Electrochemical Reduction of Aqueous CO2 to CO. *J. Mater. Chem. A* **2016**, *4*, 10710–10718.

(48) Sarfraz, S.; Garcia-Esparza, A. T.; Jedidi, A.; Cavallo, L.; Takanabe, K. Cu-Sn Bimetallic Catalyst for Selective Aqueous Electroreduction of CO2 to CO. *ACS Catal.* **2016**, *6*, 2842–2851.

(49) Zeng, J.; Bejtka, K.; Ju, W.; Castellino, M.; Chiodoni, A.; Sacco, A.; Farkhondehfal, M. A.; Hernández, S.; Rentsch, D.; Battaglia, C.; et al. Advanced Cu-Sn Foam for Selectively Converting CO2 to CO in Aqueous Solution. *Appl. Catal. B Environ.* **2018**, *236*, 475–482.

(50) Xie, H.; Chen, S.; Ma, F.; Liang, J.; Miao, Z.; Wang, T.; Wang, H.-L.; Huang, Y.; Li, Q. Boosting Tunable Syngas Formation via Electrochemical CO2 Reduction on Cu/In2O3 Core/Shell Nanoparticles. *ACS Appl. Mater. Interfaces* **2018**, *10*, 36996–37004.

(51) He, J.; Dettelbach, K. E.; Salvatore, D. A.; Li, T.; Berlinguette, C. P. High-Throughput Synthesis of Mixed-Metal Electrocatalysts for CO2 Reduction. *Angew. Chemie Int. Ed.* **2017**, *56*, 6068–6072.

(52) Hoffman, Z. B.; Gray, T. S.; Moraveck, K. B.; Gunnoe, T. B.; Zangari, G. The Electrochemical Reduction of Carbon Dioxide to Syngas and Formate at Dendritic Copper-Indium Electrocatalysts. *ACS Catal.* **2017**, *7*, 5381–5390.

(53) Rasul, S.; Anjum, D. H.; Jedidi, A.; Minenkov, Y.; Cavallo, L.; Takanabe, K. A Highly Selective Copper-Indium Bimetallic Electrocatalyst for the Electrochemical Reduction of Aqueous CO2 to CO. *Angew. Chemie Int. Ed.* **2015**, *54*, 2146–2150.

(54) Jedidi, A.; Rasul, S.; Masih, D.; Cavallo, L.; Takanabe, K. Generation of Cu–In Alloy Surfaces from CuInO2 as Selective Catalytic Sites for CO2 Electroreduction. *J. Mater. Chem. A* **2015**, *3*, 19085–19092.

(55) Larrazábal, G. O.; Martín, A. J.; Mitchell, S.; Hauert, R.; Pérez-Ramírez, J. Enhanced Reduction of CO2 to CO over Cu–In Electrocatalysts: Catalyst Evolution Is the Key. *ACS Catal.* **2016**, *6*, 6265–6274.

(56) Larrazábal, G. O.; Shinagawa, T.; Martín, A. J.; Pérez-Ramírez, J. Microfabricated Electrodes Unravel the Role of Interfaces in Multicomponent Copper-Based CO2 Reduction Catalysts. *Nat. Commun.* **2018**, *9*, 1477.

(57) Luo, W.; Xie, W.; Mutschler, R.; Oveisi, E.; De Gregorio, G. L.; Buonsanti, R.; Züttel, A. Selective and Stable Electroreduction of CO 2 to CO at the Copper/Indium Interface. *ACS Catal.* **2018**, *8*, 6571–6581.